Free-surface flow of a fluid body with an inner circular cylinder in impulsive motion

P. A. TYVAND and M. LANDRINI[1]
Department of Agricultural Engineering, Agricultural University of Norway Box 5065, N-1432 Aas, Norway
[1]*INSEAN, The Italian Ship Model Basin, Via di Vallerano 139, 00128 Roma, Italy*

Abstract. An analytical theory and numerical computations are developed for the two-dimensional free-surface flow of an initially circular layer of inviscid fluid surrounding a rigid circular cylinder. The two cylinders are initially concentric. The fluid packet is released from rest and the flow suddenly starts forced by gravity and by the simultaneous impulsive motion of the inner body. A small-time expansion of the fully nonlinear free-surface problem is developed and a closed-form solution is found up to third order for an arbitrary radius of the rigid cylinder. For the gravitational flow around the body at rest, the solution is extended up to fourth order. Free-surface profiles and hydrodynamic forces on the cylinder are calculated and discussed against numerical solutions of the exact unsteady nonlinear problem. Some basic features, such as the formation of an almost uniform layer surrounding the upstream side of the body, are captured by the theory quite well and only later on in time significant quantitative differences appear. Similarly, the behaviour of hydrodynamic loads is rather well predicted during initial stages preceding larger fluctuations observed on a longer time-scale.

Key words: cylinder, impulsive, nonlinear free surface flows, small-time expansion, boundary integral equations.

1. Introduction

The gravitational release of a packet of inviscid fluid is a classical problem in hydrodynamics, [1]. In general, one is concerned with the behaviour of an initially stagnant fluid body after its constraining walls are suddenly removed, so it flows freely due to gravity. Usually the flow is assumed to take place along a rigid horizontal bottom. This basic type of problem is called the dam-breaking problem. The dam-breaking problem is difficult due to the singularity at the fluid front: this calls for an inner expansion, which does not seem to have been developed. Probably a better insight of the physics involved in contact problems [2] could be a relevant guide also for the mathematical analysis. The analytical solution for dam breaking is known only for the outer expansion to the leading order in a small-time asymptotic series. A recent numerical-experimental work on dam breaking is presented in [3]. For the related wavemaker problem, [4], an inner expansion has been developed in [5].

The present problem is a type of gravitational release where there is no free-surface singularity. This is because the solid cylinder is completely surrounded by the free surface. In combination with the gravitational release, we also include an impulsive motion of the rigid boundary. In particular, we select the case of initially circular and concentric domain boundaries for which we are able to carry out the exact solution to third order in a small-time expansion of the full nonlinear free-surface-flow problem.

This problem is similar to that with initially flat free surface, which was studied numerically in [6] and analytically in [7], but the geometry under consideration in the present paper

is different. In impulsive-flow problems with initially flat free surface, gravitational effects enter the problem to third order in the surface elevation, [7]. In the present case, gravity affects the second-order surface deflection and the third order comprises the leading nonlinear interactions between forced flow and gravity. Gravitational self-interaction appears to fourth order.

Interaction of solid bodies with free surfaces is of importance in marine engineering applications, melting processes, and technologies which use drying or painting. The basic motivation for the present study is to provide physical insight by taking the analytical description of such an interaction as far as possible into the nonlinear regime. This goal can be reached only if one takes properly into account the geometric nonlinearity, [7], which denotes the consistent description of the finite displacement of the body away from its initial location. With geometric nonlinearity, it is possible to develop an analytical solution which reaches beyond the range where the linearized solution dominates the total solution.

With a fully analytical procedure, one has the limitation of enforcing boundary conditions at the initial domain boundaries. This is strictly valid only asymptotically as time tends to zero. Therefore, a numerical comparison with the asymptotic series is desirable. In [6], the authors checked the small-time expansion from [7]. It was demonstrated that the asymptotic series is valid even outside the range where linearized theory dominates the full solution. In the present paper, analytical and numerical methods complement each other. Since the initial flow is given in closed form, we start with a preliminary validation of the numerical method by checking both global and local quantities.

By comparing analytical and numerical findings, it appears that the analytical prediction of the free surface shape agrees well with numerical simulations for body displacements smaller than half the initial radius of the fluid body. This is true for small or moderate gravity effect, which means Froude number of order one or larger. In particular, the theory is able to capture the formation of layer of fluid with almost uniform thickness surrounding the cylinder. Further on in time, the model is unable to follow the large deformations of the free surface described by the numerical method. For gravity dominated flows, the asymptotic theory is extended further on to fourth order by including the leading term representing gravitational self-interaction. On this ground, the present theory provides also test cases to check numerical methods.

In the small-time expansion, the (second-order) hydrodynamic loads are given by a three-term series which behave linearly in time. For $t = 0^+$, the result is exact also in the context of the fully nonlinear problem. In particular, the impulsive force is given by a simple formula, while it requires special care to be recovered numerically. On a longer time-scale, the asymptotic solution deviates markedly from the numerical results already at times where the free-surface contour still follows the three-term asymptotic series relatively well. This is because there is a two-term delay in the small-time expansion of the force versus the surface. In fact, the third-order analysis for the surface produces only a first-order term for the force. We have not accomplished the calculation of the second-order force, which would have implied a full fourth-order analysis for the surface. It is believed that the two-term delay of the force expansion is the reason for its weaker convergence compared with the surface shape, for any given truncation of the small-time expansion.
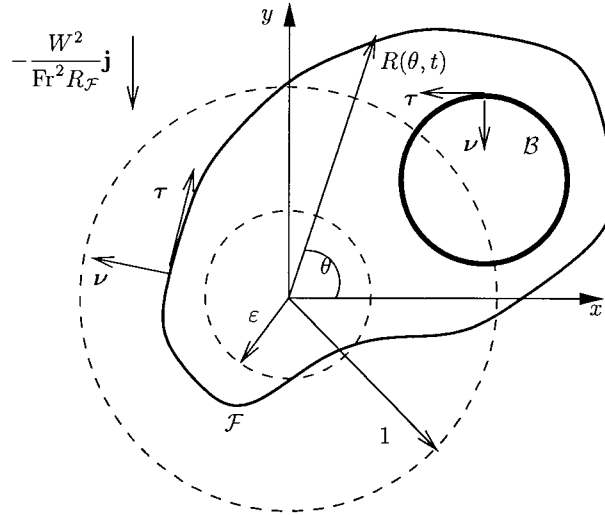
Figure 1. Sketch of problem and of nomenclature adopted. Dashed lines show the initial geometry of the flow domain.

2. Mathematical formulation

We consider a two-dimensional film of inviscid fluid with density ρ surrounding a circular cylinder $\mathcal{B}$ of radius $R_{\mathcal{B}}$.

At negative times the fluid packet is at rest, wrapped inside a circular lid of (initial) radius $R_{\mathcal{F}}$, concentric with the body. The x axis is horizontal, the y axis is vertical with origin taken in the common centers of the two boundaries. The gravitational acceleration g points in the $-y$ direction.

At time zero the wrapping is removed suddenly, so the fluid packet is released to move freely under gravity, which is mathematically equivalent to have gravity being turned on at $t = 0^{+}$. We also assume that the cylinder is put into impulsive motion at the same instant with velocity W. We introduce dimensionless equations with units of length, time, velocity, and pressure given as: $R_{\mathcal{F}}$, $R_{\mathcal{F}}/W$, W, ρW^2 and define a Froude number as: $\mathcal{F}r = W/\sqrt{g R_{\mathcal{F}}}$. The dimensionless radius of the inner (solid) cylinder is consistently defined as $\varepsilon = R_{\mathcal{B}}/R_{\mathcal{F}}$.

The inviscid flow is governed by the Laplace equation:

$$\nabla^2 \Phi = 0, \tag{1}$$

where $\Phi(x, y, t)$ is the dimensionless velocity potential. The mathematical analysis will be performed in terms of polar coordinates (r, θ), sketched in Figure 1. In particular, upon defining $\mathbf{i}$ and $\mathbf{j}$ the unit vectors in x and y directions, the position vector for a fluid particle is denoted by $\boldsymbol{r} = x\,\mathbf{i} + y\,\mathbf{j}$, the shape of the free surface $\mathcal{F}$ as a function of time by $r = R(\theta, t)$, and the location of the center of $\mathcal{B}$ by $\mathbf{R} = X(t)\,\mathbf{i} + Y(t)\,\mathbf{j}$.

Surface tension is neglected, the pressure along the free surface is taken as zero and the dimensionless kinematic and dynamic boundary conditions on the free surface can be formulated in polar coordinates as:

$$\frac{\partial R}{\partial t} + \frac{1}{R^2} \frac{\partial R}{\partial \theta} \frac{\partial \Phi}{\partial \theta} = \frac{\partial \Phi}{\partial r} \qquad r = R(\theta, t), \tag{2a}$$

$$\frac{\partial \Phi}{\partial t} + \frac{1}{2}|\nabla \Phi|^2 + \frac{1}{Fr^2}R \ \sin \theta = 0 \qquad r = R(\theta, t). \tag{2b}$$

Penney and Thornhill presented a small time expansion of these equations for a purely gravitational flow and derived the leading-order solution, [1]. In particular, this represents the singular outer solution in a matched asymptotic expansion. In the present case, the free surface motion is also forced by the moving inner cylinder, on which the kinematic condition can be written as:

$$(\boldsymbol{r} - \mathbf{R}) \cdot (\nabla \Phi - \dot{\boldsymbol{R}}) = 0, \qquad |\boldsymbol{r} - \mathbf{R}| = \varepsilon. \tag{3}$$

The dot superscript denotes time differentiation. Finally, the dimensionless pressure p is given by the Bernoulli equation:

$$p + \frac{\partial \Phi}{\partial t} + \frac{1}{2}|\nabla \Phi|^2 + \frac{1}{Fr^2}y = 0. \tag{4}$$

3. The small-time expansion

The solution of the problem for small times will be expressed as a power series in time:

$$(\Phi, R, X, Y) = (0, 1, 0, 0)$$
$$\tag{5}$$
$$+ H(t)[(\Phi_0, 0, 0, 0) + (\Phi_1, R_1, X_1, Y_1)t + (\Phi_2, R_2, X_2, Y_2)t^2 + \dots]$$

for $-\infty < t < \infty$, where we have here introduced the Heaviside unit step function:

$$H(t) = \begin{cases} 0 & t \le 0 \\ 1 & t > 0 \end{cases}. \tag{6}$$

In the following we assume a constant body velocity. Hence,

$$(X_n, Y_n) = \begin{cases} (\cos \alpha, \sin \alpha) & n = 1 \\ \\ (0, 0) & n > 1 \end{cases}, \tag{7}$$

where α denotes the angle between the direction of motion and the x-axis. We do not need to consider the case of a constant acceleration, because it is equivalent to the case of gravitational flow. In fact, the fully nonlinear boundary value problem can be readily written in a frame of reference moving with the body acceleration, say $\boldsymbol{a}$. An apparent body force $-\boldsymbol{a}$ appears which amounts in considering a modified gravity $\boldsymbol{g} - \boldsymbol{a}$. Hence, through a suitable choice of coordinate axes, the problem is formally equal to the one stated before. The Froude number is now defined using $|\boldsymbol{g} - \boldsymbol{a}|$.

To derive the free surface conditions to each order, we introduce the time differentiation operator for the free surface $r = R(\theta, t)$:

$$\left. \frac{d}{dt} \right|_{\text{f.s.}} = \frac{\partial}{\partial t} + \frac{\partial R}{\partial t}\frac{\partial}{\partial r}. \tag{8}$$

The free-surface flow is governed by the dynamic conditions to each order in time:

$$\Phi_0 = 0 \qquad\qquad r = 1, \tag{9a}$$

$$\Phi_1 = -\frac{1}{2}R_1^2 - \frac{1}{\mathrm{Fr}^2}\sin\theta \qquad\qquad r = 1, \tag{9b}$$

$$2\Phi_2 = -2R_1\frac{\partial\Phi_1}{\partial r} - R_1^2\frac{\partial^2\Phi_0}{\partial r^2} - \frac{1}{\mathrm{Fr}^2}R_1\sin\theta \qquad r = 1. \tag{9c}$$

It is interesting to observe that the Froude number enters to one order lower than in the case of an initially flat free surface [7, 8]. In the present case the gravitational acceleration acts immediately on the circular contour, while in the former case its effect is postponed until the free surface has been deformed. The kinematic free surface conditions are:

$$R_1 = \frac{\partial\Phi_0}{\partial r} \qquad\qquad r = 1, \tag{10a}$$

$$2R_2 = \frac{\partial\Phi_1}{\partial r} + R_1\frac{\partial^2\Phi_0}{\partial r^2} \qquad\qquad r = 1, \tag{10b}$$

$$6R_3 = 2\frac{\partial\Phi_2}{\partial r} + 2R_1\frac{\partial^2\Phi_1}{\partial r^2} + 2R_2\frac{\partial^2\Phi_0}{\partial r^2} + \\ + R_1^2\frac{\partial^3\Phi_0}{\partial r^3} - 2R_1'\frac{\partial\Phi_1}{\partial\theta} - 2R_1 R_1'\frac{\partial^2\Phi_0}{\partial r\partial\theta} \qquad r = 1. \tag{10c}$$

Here we have denoted the tangential derivative $d/d\theta$ by the prime ($'$). We shall see that the first-order surface deformation (10a) does not preserve mass when the amplitude is taken as finite. But the second term in the second-order deformation (10b) gives compensation for this mass deficit. At each new order in the small-time expansion the mass imbalance from lower order is repaired.

To derive the boundary conditions at the rigid cylinder we need the differential operator defined by:

$$\frac{\mathrm{d}}{\mathrm{d}t}\bigg|_{\mathrm{cyl.}} = \frac{\partial}{\partial t} + \dot{\boldsymbol{R}}\cdot\nabla. \tag{11}$$

Applying this operator recursively to Equation (3) produces the equations [7]:

$$\frac{\partial\Phi_0}{\partial r} = \cos(\theta - \alpha) \qquad\qquad r = \varepsilon, \tag{12a}$$

$$\frac{\partial\Phi_1}{\partial r} = -\frac{\partial}{\partial r}\left(\frac{\partial\Phi_0}{\partial x}\cos\alpha + \frac{\partial\Phi_0}{\partial y}\sin\alpha\right) \qquad\qquad r = \varepsilon, \tag{12b}$$

$$2\frac{\partial\Phi_2}{\partial r} = -2\frac{\partial}{\partial r}\left(\frac{\partial\Phi_1}{\partial x}\cos\alpha + \frac{\partial\Phi_1}{\partial y}\sin\alpha\right) - \\ - \frac{\partial}{\partial r}\left(\frac{\partial^2\Phi_0}{\partial x^2}\cos^2\alpha + \frac{\partial^2\Phi_0}{\partial x\partial y}\sin 2\alpha + \frac{\partial^2\Phi_0}{\partial y^2}\sin^2\alpha\right) \qquad r = \varepsilon. \tag{12c}$$

One must be cautious with such a mixture of partial derivatives in Cartesian and polar co-ordinates, as they are not mutually commutative. The inhomogeneous terms in the two last equations express the geometric nonlinearity, [7]. This is a consistent way of taking into account the finite displacement of a body away from its initial position. All inhomogeneous terms are formally linear in the differential equations at each order of a small-time expansion. Still the second- and third-order derivatives in Equations (12b, 12c) represent nonlinear terms (quadratic and cubic) in a spatial Taylor expansion. The geometric nonlinearity extends the validity of a closed-form analytical solution beyond the limit where the linearized solution dominates the full solution. Without geometric nonlinearity, one would be left with a linearized description at the inner boundary, with a nonzero normal velocity only in the leading-order kinematic condition.

Consistently with the time expansion (5), the dimensionless force acting on the rigid cylinder is expanded as:

$$F(t) = F_{-1}\delta(t) + H(t)(F_0 + F_1 t + F_2 t^2 + \dots), \tag{13}$$

$\delta(t)$ being the Dirac delta function. The unit of dimensionless force, measured per unit length along the cylinder axis, is $\rho R_{\mathcal{F}} W^2$,

3.1. THE ZEROTH-ORDER POTENTIAL

The zeroth-order potential is governed by a Type II boundary-value problem, as given in the Appendix A. Therefore, its solution is:

$$\Phi_0 = \varepsilon^2 \frac{r - r^{-1}}{1 + \varepsilon^2} \cos(\theta - \alpha), \tag{14}$$

and the resulting first-order deformation of the free surface reads:

$$R_1 = \frac{2\varepsilon^2}{1 + \varepsilon^2} \cos(\theta - \alpha). \tag{15}$$

Within a strictly linear theory, the circular shape may be considered as intact and a pure translation of the surface in the direction of motion of the cylinder is allowed. In particular, the center of the fluid packet is displaced from the origin to the point

$$(x_1, y_1)t = \frac{2\varepsilon^2}{1 + \varepsilon^2} (\cos \alpha, \ \sin \alpha)t, \tag{16}$$

which means that, to first order, the fluid packet follows the same direction of motion as the cylinder, but covers a somewhat shorter distance:

$$\frac{x_1}{X_1} = \frac{y_1}{Y_1} = \frac{2\varepsilon^2}{1 + \varepsilon^2}. \tag{17}$$

As an example, the net surface velocity is just one half of the cylinder velocity when the cylinder size is $\varepsilon = 1/\sqrt{3} \simeq 0.57735$.

The impulsive force of the fluid packet acting on the cylinder is:

$$F_{-1} = -\pi \varepsilon^2 \frac{1 - \varepsilon^2}{1 + \varepsilon^2} \frac{W}{W}. \tag{18}$$
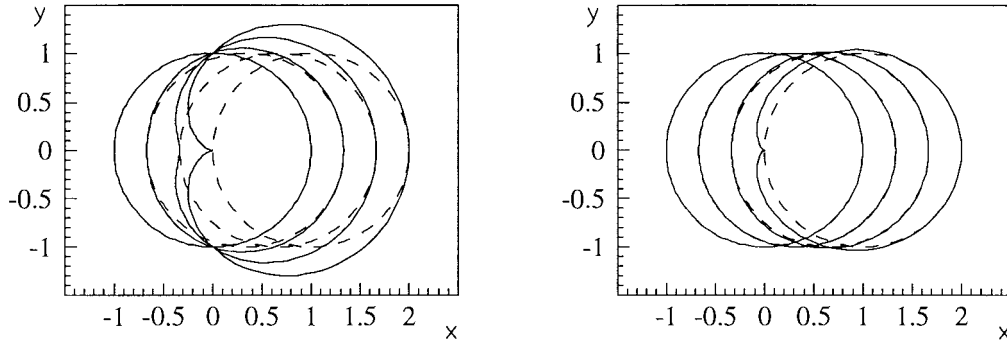
Figure 2. Free surface contours (solid lines) for the limit case $\varepsilon = 1$ and horizontal motion, $\alpha = 0$, with unit velocity from left to right. Snapshots given at times $t = 0, \frac{1}{3}, \frac{2}{3}, 1$. The exact solution is given by the dashed lines at the same time instants. Left: solution to first order in time. Right: solution up to second order in time; actually this solution is accurate to third order in time because the term R_3 (cf. Equation (46)) is zero for $\varepsilon = 1$.

and points always in the direction opposite of the motion. This force represents the dimensionless added momentum of the cylinder in motion. The added mass relative to the displaced fluid mass of the impulsively moving cylinder in unbounded domain is given by:

$$\frac{|F_{-1}|}{\pi \varepsilon^2} = \frac{1 - \varepsilon^2}{1 + \varepsilon^2}. \tag{19}$$

This relative added mass decreases monotonously with increasing radius. It is obviously equal to one in unbounded fluid domain and tends to zero in the thin layer limit.

In the rest of this paper finite amplitude displacements are considered. The area inside the fluid packet according to first-order theory amounts to:

$$A = \frac{1}{2} \int_0^{2\pi} R^2(\theta, t) \, \mathrm{d}\theta = \pi \left(1 + \frac{2\varepsilon^4}{(1 + \varepsilon^2)^2} t^2 \right). \tag{20}$$

So the first-order solution conserves mass at first order but generates a second-order imbalance. This second-order mass deficit will be compensated by a constant contribution to R_2.

The thin-layer limit, $\varepsilon \to 1$, is a useful reference case for studying the convergence of the small-time expansion because the exact solution is simply the translated circle. In the left-hand plot of Figure 2, for increasing time, the deformed fluid packet to first order (solid lines) is compared with the exact solution (dashed lines). A clue for identifying each curve is that all surface points are correct along the x axis. For $t = \frac{1}{3}$, the first-order free surface already differs from the exact contour. As time increases, a cusp develops for $t = 1$, and an unphysical loop (not shown) appears later on. Therefore, the asymptotic series does not make sense for $t > 1$. Also the mass imbalance increases rapidly with time. The fact that the exact solution is the translated circle is verified in Appendix B where the small-time expansion is carried out in a coordinate system moving with the solid cylinder.

3.2. THE FIRST-ORDER POTENTIAL

We will now derive the first-order potential and its corresponding second-order deformation of the free surface. Following [7], the first-order potential will be written by superposition as:

$$\Phi_1 = \phi_1 + \psi_1 + \varphi_1^{(\text{Fr})}, \tag{21}$$

where the first two terms are due to the free surface nonlinearity and to geometric nonlinearity respectively, and the last term with superscript (Fr) is the gravity-dependent term.

The potential due to the free surface nonlinearity obeys the conditions:

$$\phi_1 = -\frac{1}{2}R_1^2 \quad r = 1, \qquad \frac{\partial \phi_1}{\partial r} = 0 \quad r = \varepsilon, \tag{22}$$

and, disregarding an insignificant constant, the solution is:

$$\phi_1 = -\frac{r^2 + \varepsilon^4 r^{-2}}{(1 + \varepsilon^{-2})^2 (1 + \varepsilon^4)} \cos 2(\theta - \alpha). \tag{23}$$

The potential due to geometric nonlinearity is defined by:

$$\psi_1 = 0 \quad r = 1, \qquad \frac{\partial \psi_1}{\partial r} = -\frac{\partial}{\partial r}\frac{\partial \Phi_0}{\partial x} \quad r = \varepsilon. \tag{24}$$

In Equation (12b) we have temporarily set $\alpha = 0$ in order to simplify the analysis. This is valid provided θ will be eventually replaced by $(\theta - \alpha)$. The final general solution is:

$$\psi_1 = \frac{r^2 - r^{-2}}{(1 + \varepsilon^{-2})(1 + \varepsilon^4)} \cos 2(\theta - \alpha). \tag{25}$$

The gravity-dependent potential with zero normal derivative at the cylinder is given by:

$$\varphi_1^{(Fr)}(r, \theta) = -\frac{1}{Fr^2}\frac{r + \varepsilon^2 r^{-1}}{1 + \varepsilon^2} \sin \theta, \tag{26}$$

which gives the following contribution to the second-order deformation:

$$R_2^{(Fr)} = -\frac{1}{2Fr^2}\frac{1 - \varepsilon^2}{1 + \varepsilon^2} \sin \theta. \tag{27}$$

Let us first interpret this result in terms of infinitesimal disturbances. Then the circular shape is intact, and the center of the fluid packet is effectively translated to the point $(0, y_2^{(Fr)}t^2)$ given by:

$$y_2^{(Frs)} = -\frac{1}{2Fr^2}\frac{1 - \varepsilon^2}{1 + \varepsilon^2}. \tag{28}$$

The acceleration of the fluid packet relative to the gravitational acceleration is:

$$2y_2^{(Fr)} Fr^2 = \frac{1 - \varepsilon^2}{1 + \varepsilon^2}. \tag{29}$$

When the inner cylinder radius tends to zero, the packet is falling freely. When it tends to one, however, there is no net gravitational motion. The fluid surface starts falling with half the gravitational acceleration when $\varepsilon = 1/\sqrt{3}$. This happens to be the same value as the one for which the initial packet velocity is one half the forced velocity. We also note the similarity between Equations (19) and (20): the first-order relative added mass (relative to the displaced mass) is the same as the leading-order surface acceleration (relative to gravity).

By Equation (10b) the basic contribution to the second-order deformation is the radial derivative of the three terms (21). But there is an additional term compensating for the mass deficit (20) in the first-order deformation:

$$\frac{1}{2} R_1 \frac{\partial^2 \Phi_0}{\partial r^2} = -\frac{2}{(1 + \varepsilon^{-2})^2} \, \cos^2(\theta - \alpha) \quad r = 1. \tag{30}$$

This contains the only angle-independent contribution to the second-order deformation. The second-order deformation due to the first-order potential is:

$$\frac{1}{2} \frac{\partial \Phi_1}{\partial r} = \frac{(2 - \varepsilon^2 + \varepsilon^4)}{(1 + \varepsilon^{-2})(1 + \varepsilon^4)} \, \cos 2(\theta - \alpha) - \frac{1}{\mathrm{Fr}^2} \frac{1 - \varepsilon^2}{1 + \varepsilon^2} \, \sin \theta \quad r = 1. \tag{31}$$

The total second-order deformation is the sum of Equations (30) and (31):

$$R_2 = -\frac{\varepsilon^4}{(1 + \varepsilon^2)^2} + \frac{2\varepsilon^2}{(1 + \varepsilon^2)^2 (1 + \varepsilon^4)} \, \cos 2(\theta - \alpha) - \frac{1}{2\mathrm{Fr}^2} \frac{1 - \varepsilon^2}{1 + \varepsilon^2} \, \sin \theta. \tag{32}$$

The right-hand plot in Figure 2 shows the contour shape to second-order, for the limit case $\varepsilon \to 1$ of vanishing fluid film. Upon comparing with the first-order solution on the left-hand plot, the second-order curves appear to be much better approximations and differences with respect to the exact solution are (graphically) evident only for $t > 0.5$. Figure 2 illustrates the merits of geometric nonlinearity in the second-order solution. We start with the left-hand plot of the first-order solution, which is governed solely by a normal velocity ($\cos \theta$) pumped through the fixed contour $r = 1$. Then the right-hand plot shows how the inadequate first-order solution is improved by adding the second-order deformation due to geometric nonlinearity plus the mass compensation term given by Equation (30).

The only nonzero contribution to the zeroth-order force is due to gravity. In the submerged cylinder problem gravity does not enter the force to zeroth-order, but only to first order in time. In the present case we find the vertical zeroth-order force on the cylinder from the falling fluid film to be:

$$\boldsymbol{F}_0 = \boldsymbol{F}_0^{(\mathrm{Fr})} = -\frac{\pi}{\mathrm{Fr}^2} \frac{\varepsilon^2 (1 - \varepsilon^2)}{1 + \varepsilon^2} \, \mathbf{j}. \tag{33}$$

In dimensional variables the absolute value of this downward gravitational force is:

$$F^\star = G^\star \frac{1 - R_{\mathcal{B}}^2 / R_{\mathcal{F}}^2}{1 + R_{\mathcal{B}}^2 / R_{\mathcal{F}}^2}. \tag{34}$$

Here we have introduced the Archimedes force $G^\star = \pi \rho g a^2 L$, which is the weight of the fluid displaced by a rigid cylinder of length L. The ratio $F^\star / G^\star$ is equal to the ratio between the impulsive added mass and the displaced fluid mass for forced motion (18). We will show that this is not a coincidence. There are basic relationships between impulsive flows with constant velocity and constant acceleration. This has been demonstrated in [7, Section 10], where the relevant transformation equations are developed (although their higher-order transformations are erroneous). We will now recapitulate the leading-order analysis of [7] for our circular geometry. If we replace a constant impulsive velocity by a constant impulsive acceleration, we make the transformation $(X_1, Y_1) \to 2(X_2, Y_2)$. This corresponds to defining as velocity scale $W = \sqrt{a^\star R_{\mathcal{F}}}$ where $a^\star$ is the dimensional acceleration of the cylinder. The dimensionless forced acceleration is thereby unity. The leading-order displacement and force for constant acceleration are then given by these quantities for constant velocity:

$$R_2 = \frac{1}{2} R_1 \qquad \boldsymbol{F}_0 = \boldsymbol{F}_{-1}. \tag{35}$$

This shows why the formulas (18) and (33) are the same when the Froude number is unity by definition. We will finally compare the surface deformation for the cases of impulsive accelerated cylinder and purely gravitational flow. The latter case is described above by Equation (32), if we neglect all non-gravitational terms and put Fr $= 1$. To compare this with Equation (35), we have to change coordinate system by following the accelerating cylinder. Let us take $\alpha = \pi/2$ so the motion is upwards. Then the surface deformation due to gravity will be equivalent to the surface deformation (35) due to an accelerated cylinder minus $(\sin\theta)/2$ due to the change of coordinate system. This produces the second-order deformation due to gravitational flow, according to the transformation (35):

$$R_2 = \frac{1}{2}(R_1 - \sin\theta) = -\frac{1}{2}\frac{1-\varepsilon^2}{1+\varepsilon^2}\,\sin\theta. \tag{36}$$

This is equivalent with the gravitational term in Equation (32), taking the Froude number as unity. Thereby, we have verified that the impulsively accelerated cylinder is equivalent to a purely gravitational flow at the leading order as $t \to 0$.

3.3.   THE SECOND-ORDER POTENTIAL

We write the second-order potential as the sum:

$$\Phi_2 = \phi_2 + \psi_2 \tag{37}$$

The first term is the potential due to free-surface nonlinearity and is given by the non-homogeneous condition (9c) at the free surface:

$$\phi_2 = \frac{\varepsilon^4(\varepsilon^6 + \varepsilon^2 - 4)}{(1+\varepsilon^2)^3(1+\varepsilon^4)}\,\cos(\theta-\alpha) - \frac{\varepsilon^4(\varepsilon^6 + \varepsilon^2 + 4)}{(1+\varepsilon^2)^3(1+\varepsilon^4)}\,\cos 3(\theta-\alpha) -$$
$$-\frac{1}{2\mathrm{Fr}^2}\frac{\varepsilon^2(3\varepsilon^2-1)}{(1+\varepsilon^2)^2}(\sin\alpha + \sin(2\theta-\alpha)) \qquad r = 1, \quad \text{(38a)}$$

with zero normal derivative at the cylinder contour:

$$\frac{\partial\phi_2}{\partial r} = 0 \quad r = \varepsilon. \tag{38b}$$

From Equation (A3) in Appendix A, we find that the normal derivative at the surface is:

$$\frac{\partial\phi_2}{\partial r} = \frac{\varepsilon^4(1-\varepsilon^2)(\varepsilon^6+\varepsilon^2-4)}{(1+\varepsilon^2)^4(1+\varepsilon^4)}\,\cos(\theta-\alpha) -$$
$$-3\frac{\varepsilon^4(1-\varepsilon^6)\,(\varepsilon^6+\varepsilon^2+4)}{(1+\varepsilon^6)\,(1+\varepsilon^2)^3\,(1+\varepsilon^4)}\,\cos 3(\theta-\alpha) - \tag{39}$$
$$-\frac{1}{\mathrm{Fr}^2}\frac{\varepsilon^2\,(3\varepsilon^2-1)\,(1-\varepsilon^2)}{(1+\varepsilon^2)\,(1+\varepsilon^4)}\,\sin(2\theta-\alpha), \qquad r = 1.$$

This expression divided by three is the free-surface nonlinearity contribution to the third-order surface deformation. The last term represents the leading nonlinear free-surface interaction between gravity and the forced motion. We note that this contribution changes sign at a certain radius $\varepsilon = 1/\sqrt{3}$. This has been identified above as the case where the initial surface motion is half the forced motion.

The second term in Equation (37), ψ_2, is the potential due to geometric nonlinearity: it is zero at the free surface and obeys a non-homogeneous condition (12c) at the body. We can find the solution by integrating out the first radial dependence from the boundary condition [7]:

$$\overset{\star}{\psi}_2 = -\frac{\partial \Phi_1}{\partial x} \cos \alpha - \frac{\partial \Phi_1}{\partial y} \sin \alpha -$$

$$-\frac{1}{2} \left(\frac{\partial^2 \Phi_0}{\partial x^2} \cos^2\alpha + \frac{\partial^2 \Phi_0}{\partial x \partial y} \sin 2\alpha + \frac{\partial^2 \Phi_0}{\partial y^2} \sin^2\alpha \right). \tag{40}$$

This tedious differentiation, carried out using MATHEMATICA, gives the formula:

$$\overset{\star}{\psi}_2 = -\frac{\varepsilon^2(1 + \varepsilon^2 - \varepsilon^4 + \varepsilon^6)}{(1 + \varepsilon^2)^2 (1 + \varepsilon^4) r^3} \cos 3(\theta - \alpha) - \frac{2\varepsilon^2 r}{(1 + \varepsilon^2)^2(1 + \varepsilon^4)} \cos (\theta - \alpha) -$$

$$-\frac{1}{\text{Fr}^2} \frac{\sin (2\theta - \alpha)}{(1 + \varepsilon^{-2}) r^2} + \frac{1}{\text{Fr}^2} \frac{\sin \alpha}{(1 + \varepsilon^2)}. \tag{41}$$

This contribution, marked with a star $\star$, is not the full solution ψ_2. A correction potential $\tilde{\psi}_2$ must be added to account for the homogeneous condition ($\psi_2 = 0$) at the outer boundary. For this purpose, we first rewrite Equation (41) by deleting the constant term not contributing to the final solution:

$$\overset{\star}{\psi}_2 = -\varepsilon^2 \frac{(1 + \varepsilon^2 - \varepsilon^4 + \varepsilon^6)r^{-3} \cos 3(\theta - \alpha) + 2r \cos (\theta - \alpha)}{(1 + \varepsilon^2)^2(1 + \varepsilon^4)} -$$

$$-\frac{1}{\text{Fr}^2} \frac{\varepsilon^2 \sin (2\theta - \alpha)}{(1 + \varepsilon^2) r^2}. \tag{42}$$

The correction potential, with zero normal derivative at the inner cylinder and the Dirichlet condition:

$$\tilde{\psi}_2 = \varepsilon^2 \frac{(1 + \varepsilon^2 - \varepsilon^4 + \varepsilon^6) \cos 3(\theta - \alpha) + 2 \cos (\theta - \alpha)}{(1 + \varepsilon^2)^2(1 + \varepsilon^4)} +$$

$$+\frac{1}{\text{Fr}^2} \frac{\varepsilon^2 \sin (2\theta - \alpha)}{1 + \varepsilon^2} \quad r = 1 \tag{43}$$

at the free surface, is found from the solution of Type I problem in Appendix A. On this ground, we finally obtain the normal derivative of the second-order potential due to geometric nonlinearity:

$$\frac{\partial \psi_2}{\partial r} = \frac{6\varepsilon^2(1 + \varepsilon^2 - \varepsilon^4 + \varepsilon^6)}{(1 + \varepsilon^2)^3 (1 + \varepsilon^4) (1 - \varepsilon^2 + \varepsilon^4)} \cos 3(\theta - \alpha) -$$

$$\frac{4\varepsilon^4}{(1 + \varepsilon^2)^3(1 + \varepsilon^4)} \cos (\theta - \alpha) \qquad\qquad r = 1, \tag{44}$$

$$+\frac{4\varepsilon^2}{\text{Fr}^2(1 + \varepsilon^2)(1 + \varepsilon^4)} \sin (2\theta - \alpha)$$

by summing $\partial \tilde{\psi}_2 / \partial r$, following from Equation (A3), and the normal derivative of the potential $\overset{\star}{\psi}_2$. We add formula (39) to the last equation and find the normal derivative of the total second-order potential:

$$\frac{\partial \Phi_2}{\partial r} = 3\varepsilon^2 \frac{2 - \varepsilon^4 + 5\varepsilon^8 + \varepsilon^{10} + \varepsilon^{14}}{(1 + \varepsilon^2)^4 (1 + \varepsilon^4)(1 - \varepsilon^2 + \varepsilon^4)} \cos 3(\theta - \alpha) -$$

$$-\varepsilon^4 \frac{8 - \varepsilon^2 + \varepsilon^4 - \varepsilon^6 + \varepsilon^8}{(1 + \varepsilon^2)^4 (1 + \varepsilon^4)} \cos (\theta - \alpha) + \qquad r = 1. \qquad (45)$$

$$+\frac{1}{\text{Fr}^2} \varepsilon^2 \frac{5 - 4\varepsilon^2 + 3\varepsilon^4}{(1 + \varepsilon^2)(1 + \varepsilon^4)} \sin (2\theta - \alpha).$$

From the boundary condition (10c) we find the third-order deformation of the surface:

$$R_3 = 2\frac{\varepsilon^2(1 - \varepsilon^2)(1 - \varepsilon^4 - \varepsilon^6)}{(1 + \varepsilon^2)^4 (1 + \varepsilon^4)(1 - \varepsilon^2 + \varepsilon^4)} \cos 3(\theta - \alpha) -$$

$$-\frac{2}{3} \frac{\varepsilon^4(1 - \varepsilon^2)(7 + 7\varepsilon^2 + 5\varepsilon^4 + 2\varepsilon^6)}{(1 + \varepsilon^2)^4 (1 + \varepsilon^4)} \cos (\theta - \alpha) + \qquad (46)$$

$$+\frac{1}{6\text{Fr}^2} \frac{\varepsilon^2(1 - \varepsilon^2)(9 + 4\varepsilon^2 + \varepsilon^4)}{(1 + \varepsilon^2)^2 (1 + \varepsilon^4)} \sin (2\theta - \alpha) + \frac{1}{2\text{Fr}^2} \frac{\varepsilon^2(1 - \varepsilon^2)}{(1 + \varepsilon^2)^2} \sin \alpha.$$

The third-order deformation vanishes in the limit $\varepsilon \to 1$. This means that the curves in the right-hand plot of Figure 2 show the deviation between the exact contour for a fluid film of vanishing thickness and our third-order small-time expansion.

We note that the gravity-dependent terms express the leading-order nonlinear interaction between gravity and the forced flow. The purely gravitational self-interaction will enter the nonlinear problem in the fourth-order deformation.

In order to calculate the first-order force we need the formula:

$$\boldsymbol{F} = -\varepsilon \int_0^{2\pi} [(p)_{r=\varepsilon} + t\boldsymbol{R}_1 \cdot (\nabla p)_{r=\varepsilon} + O(t^2)] \mathbf{i}_r \, d\theta. \qquad (47)$$

The radial unit vector is $\mathbf{i}_r$. Here the second term in the integrand gives the leading effect of finite displacement of the cylinder. It arises from a Taylor expansion with respect to the cylinder position, and contributes to the first-order force. The impulsive force and the zeroth-order force are not influenced by the second term in this integrand.

Calculating the first-order force from Equation (47) gives zero gravitational contribution. With no gravitational effect, it follows that the force points in the direction of motion, and the calculation can be simplified somewhat by putting $\alpha = 0$. The calculation, performed using MATHEMATICA, produces the following formula for the first-order force:

$$\boldsymbol{F}_1 = 4\pi \frac{\varepsilon^4(1 - 3\varepsilon^2 + \varepsilon^4 + \varepsilon^8)}{(1 + \varepsilon^2)^4 (1 + \varepsilon^4)} \frac{\boldsymbol{W}}{W}, \qquad (48)$$

which will be discussed in the following.

4. Numerical solution of the exact problem

To discuss the time-range of validity of the analytical solution and study the flow further on, we also adopt a numerical technique to solve the exact problem stated in Section 2. The fluid motion is described through an initial value problem for the Euler equations

$$\nabla \cdot \boldsymbol{u} = 0 \quad \frac{\mathrm{D}\boldsymbol{u}}{\mathrm{D}t} = -\frac{1}{\rho}\nabla p + \boldsymbol{g}, \tag{49}$$

with the no-penetration condition

$$(\boldsymbol{u} - \boldsymbol{W}) \cdot \boldsymbol{v} = 0 \tag{50}$$

on the body $\mathcal{B}$ and, respectively, the kinematic and dynamic boundary conditions

$$\frac{\partial \boldsymbol{P}(\xi, t)}{\partial t} = \boldsymbol{u} \quad \frac{\partial u_\xi(\xi, t)}{\partial t} = \frac{\partial}{\partial \xi}\left(\frac{1}{2}u_\xi^2 - gy\right) \tag{51}$$

on the free surface $\mathcal{F}$. In (51), the free surface is described in the form $\boldsymbol{P}[x(\xi, t), y(\xi, t)]$, ξ being a Lagrangian parameter, and u_ξ the covariant component of $\boldsymbol{u}|_{\mathcal{F}}$ along the tangential vector $\partial \boldsymbol{P}/\partial \xi$. The initial conditions are above stated.

The unsteady fully nonlinear problem is numerically solved through a boundary integral approach coupled with a time marching procedure. The velocity field is expressed by

$$\boldsymbol{u}(\boldsymbol{Q}) = \nabla_Q \int_{\mathcal{F}} \boldsymbol{u} \cdot \boldsymbol{v} G \, \mathrm{d}S_P + \nabla_Q \times \int_{\mathcal{F}} \boldsymbol{u} \times \boldsymbol{v} \, G \, \mathrm{d}S_P + \nabla_Q \int_{\mathcal{B}} \sigma \, G \, \mathrm{d}S_P, \tag{52}$$

where the influence of the free surface is given 'directly' in terms of the normal $\boldsymbol{u} \cdot \boldsymbol{v}$ and tangential $\boldsymbol{u} \times \boldsymbol{v}$ velocity components on $\mathcal{F}$, while the body is represented by a source distribution σ. G is the two-dimensional free space Green function.

The normal velocity component on $\mathcal{B}$ is explicitly known by Equation (50), while u_ξ is assumed to be known at a given instant of time. The still unknown velocity component $\boldsymbol{u} \cdot \boldsymbol{v}|_{\mathcal{F}}$ and the source strength σ can be evaluated by solving the integral equations following from (52) when $\boldsymbol{P} \in \partial\Omega \equiv \mathcal{F} \cup \mathcal{B}$ and taking the normal projection. In principle, an integral representation for the velocity field in terms of velocity components on $\mathcal{F}$ and on $\mathcal{B}$ can be adopted, [9]. In this case the resulting integral equation has an eigensolution related to the circulation around the body and the resulting algorithm would be less efficient (see [10] for zero circulation cases, and [9] for lifting bodies). The drawback of the adopted hybrid formula is that the velocity on the body, if required, has to be evaluated a posteriori using the tangential projection of (52).

Once the velocity field on $\mathcal{F}$ is evaluated, the solution can be prolonged in time by the free surface evolution equations (51). Eventually, new geometry and boundary data are obtained and the procedure can be re-initialized. A standard fourth-order Runge–Kutta scheme is used for time marching.

The contour integrals are discretized by the Euler–Mclaurin summation formula which, in combination with trigonometric polynomials, allows us to achieve a spectral convergence to the (assumed) C^∞-solution, [11]. The linear algebraic system obtained is solved by an iteration technique [12]. In this case an operation count of order N^2, the total number of unknowns, is obtained together with a storage requirements proportional to N^2. Without reducing the accuracy, for larger N, multipoles expansion and fast summation techniques can be expediently applied to achieve a computational effort of order $N \log N$ and a storage requirement just of order N. The algorithm is fully described by [13].

Few comments are useful about the computation of the fluid force and moment:

$$\boldsymbol{F} = \int_{\mathcal{B}} p\boldsymbol{v} \, \mathrm{d}S \quad \boldsymbol{M} = \int_{\mathcal{B}} p\,\boldsymbol{r} \times \boldsymbol{v} \, \mathrm{d}S.$$

As pointed out in [14], the Eulerian derivative of the velocity potential, $\dot{\Phi}$, is a harmonic function and the vector field $\dot{\boldsymbol{u}} = \nabla\dot{\Phi}$ satisfies the boundary condition:

$$\dot{u}_\xi = \frac{\partial}{\partial\xi}\left(-\tfrac{1}{2}u^2(\xi, t) - g\eta(\xi, t)\right) \tag{53}$$

on the free surface $\mathcal{F}$, and:

$$\dot{u}_\nu = (\dot{\boldsymbol{W}}_O + \dot{\boldsymbol{\Omega}} \times \boldsymbol{OP} - \Omega^2\boldsymbol{OP}) \cdot \boldsymbol{v} - \Omega\boldsymbol{\tau} \cdot (\boldsymbol{W} - \boldsymbol{u}) -$$

$$-W_\tau\partial_\tau(\boldsymbol{u} \cdot \boldsymbol{v}) + W_\nu\partial_\tau(\boldsymbol{u} \cdot \boldsymbol{\tau}) - \frac{\boldsymbol{W} \cdot \boldsymbol{u}}{\mathcal{R}} \tag{54}$$

on the body $\mathcal{B}$. In Equation (54), a rigid body motion of the form $\boldsymbol{W}_P = \boldsymbol{W}_O(t) + \boldsymbol{\Omega}(t) \times (\boldsymbol{P} - \boldsymbol{O})$ is considered, though the angular velocity $\boldsymbol{\Omega}$ is zero in our problem, and $\mathcal{R}$ is the radius of curvature of $\mathcal{B}$ at $\boldsymbol{P}$. Hence a boundary integral problem, formally equivalent to the one solved for the velocity, can be solved with a small extra computational effort.

Once this is accomplished, $\dot{u}_\tau = \partial\dot{\Phi}/\partial\tau$ on the body contour can be integrated by a spectral technique to get $\dot{\Phi}$ and, ultimately, the pressure (4).

We note, in passing, that similar boundary value problems can be written down for successive time derivatives and that a Taylor expansion technique could be adopted to step forward the solution in time [14, 15]. A possible advantage would be a smaller computational effort with respect to a fourth-order Runge–Kutta scheme because the integral equations has to be discretized once each time step, i.e the operation count is roughly reduced from $4 \times N^2$ to N^2 per time step. This is not valid anymore for the present accelerated solver which, regardless the adopted time marching procedure, requires about $4 \times N \log N$ operations. The Taylor expansion scheme probably has better stability properties. We eventually adopted the Runge–Kutta scheme because of its simpler coding, more evident when solid boundaries in arbitrary motion are also present. Sawtooth instabilities, firstly reported in [16], are removed by the filtering technique described in [15].

4.1. VALIDATION OF THE NUMERICAL METHOD

All the solutions shown in the following are obtained by systematically refining the relevant discrete parameters. Usually, the total number N of points on $\partial\Omega$ is doubled and the time step Δt halved until convergence is achieved for the total simulation time considered.

A first analysis of the convergence properties of the boundary integral equation solver is performed by comparing solutions obtained for $t = 0$ with analytical results from previous sections. In particular, the velocity field $\nabla\Phi_0$ gives the exact solution of the boundary value problem at hand at $t = 0$. A similar problem has been used in [13] to discuss the convergence properties of the present algorithm and, therefore, it is not reproduced here. We will use, instead, the force $\boldsymbol{F}_0$, Equation (33), to check both the properties of the boundary integral equation solver and the procedure for computing hydrodynamic loads. As an example, the comparison of numerical solutions for circular cylinders of increasing radius ε against analytical values is given in Table 1. With a relatively coarse discretization ($N_\mathcal{F} = N_\mathcal{B} = 64$) a good accuracy is obtained for $\varepsilon < 0.9$. Even for $\varepsilon = 0.8$ the predicted value of F_0 agrees with the analytical one up to the first eleven significant digits. By doubling the number of the discrete points an accuracy up to 14 digits is recovered (result not shown). Further refinements are probably counter balanced by round-off and truncation errors but no attempt to use quadruple

Table 1. Numerical prediction of F_0 for ε approaching 1 and Fr $= 1$. For radii ranging from 0·01 to 0·8 (upper part of the table) the numerical solution is obtained by using $N_{\mathscr{F}} = N_{\mathscr{B}} = 64$. For larger radii (lower part) the circular cylinder and the free surface are discretized by the same number of points reported in the left-hand column. The analytical results follow from Equation (33).

ε	0.01	0.05	0.1
Numerical	−0·0003140964397884628	−0·007814809655750250	−0·03079382898073159
Analytical	−0·0003140964397884645	−0·007814809655750174	−0·03079382898073164
ε	0.2	0.4	0.8
Numerical	−0·1159972672094692	−0·3639914246917828	−0·4413554557248014
Analytical	−0·1159972672094693	−0·3639914246917829	−0·4413554557238342

	ε		
$N_{\mathscr{F}}, N_{\mathscr{B}}$	0·90	0·95	0·99
64	−0·2671260788423800	−0·1498385229352068	−2·201377591264447
128	−0·2671221598880131	−0·1453097475110785	−0·4209423929073617
256	−0·2671221598825805	−0·1453038205435533	−5·195585379529581E − 02
512	−0·2671221598825806	−0·1453038205318372	−3·105142817997401E − 02
1024	−0·2671221598825757	−0·1453038205318309	−3·094469914902595E − 02
2048	−0·2671221598825771	−0·1453038205318322	−3·094469557077086E − 02
Analytical	−0·2671221598825796	−0·1453038205318355	−3·094469557077363E − 02

precision has been made because the achieved degree of accuracy is satisfactory enough for the present purposes. As expected more critical conditions occur for larger values of ε, reported in the lower part of Table 1. For fixed $N_{\mathscr{F}} + N_{\mathscr{B}}$, the accuracy decreases as the radius increases and, eventually, the coarsest grid provides a completely wrong result for the smallest thickness of the fluid layer ($\varepsilon = 0.99$) which is in this case about ten times smaller than the spacing between the points on the boundary ($2\pi R_{\mathscr{F}}/N_{\mathscr{F}} \simeq 0.098$). This behaviour is due to the relatively poor discretization of non-singular contour integrals when field points are close but not belonging to the considered contour, [17]. Also in this case, a good agreement with the exact value is rapidly recovered by refining enough the discretization.

On this ground, it is expected that the accuracy of the numerical solution diminishes in time as the boundaries approach each other. This will be further evidenced by looking at mass and energy evolution of the system and at the behaviour of the computed forces. In particular, the conservation of total mass and rate of change of mass,

$$M = \int_{\mathscr{F} \cup \mathscr{B}} y \, \mathrm{d}x \qquad M_t = \int_{\mathscr{F} \cup \mathscr{B}} \boldsymbol{u} \cdot \boldsymbol{v} \, \mathrm{d}x, \tag{55}$$

are controlled in time and the power exchange due to the body motion,

$$W = \int_{\mathscr{B}} p \boldsymbol{v} \cdot \boldsymbol{u} \, \mathrm{d}S = \int_{\mathscr{B}} p \boldsymbol{W} \cdot \boldsymbol{v} \, \mathrm{d}S, \tag{56}$$

is compared with the rate of change of the total energy of the fluid,

$$E_t = \frac{d}{dt} \left[\frac{1}{2} \rho \int_{\mathscr{F} \cup \mathscr{B}} \varphi \, \boldsymbol{u} \cdot \boldsymbol{v} \, \mathrm{d}S + \frac{1}{2} \rho g \int_{\mathscr{F} \cup \mathscr{B}} y^2 \, \mathrm{d}x \right]. \tag{57}$$

Table 2. Main discretization parameters for the results of Figures 3–5. $N_{\mathcal{F}}$: number of free surface Lagrangian markers, $N_{\mathcal{B}}$: number of points on the body, Δt: time step adopted within a fourth-order Runge–Kutta procedure.

	a	b	c	d	e	f
$N_{\mathcal{F}}$	64	128	256	512	1024	2048
$N_{\mathcal{B}}$	32	64	128	256	256	256
Δt	0·01	0·005	0·0025	0·0025	0·0025	0·0025

In the last equation, the velocity potential on the boundary is evaluated by integrating the tangential velocity component. This can be effectively achieved by spectral techniques with accuracy consistent with that of the whole numerical procedure. Actually, the potential is determined but a constant value which is not relevant because the flux across each single boundary is zero. All contour integrals in formulas above are treated by the trapezoidal rule which is known to have spectral convergence for smooth periodic integrands.

We discuss the performances of the method by considering a solid cylinder with radius $\varepsilon = 0·5$ suddenly set in horizontal motion from left to right, with a resulting Froude number $\mathrm{Fr} = 1$. In the next section this case will be referred to as Case II.

The evolution in time of the fluid domain is shown in Figure 3, where the free surface is deformed under the combined action of body and gravity. The simulation ends with the formation of a thin layer of fluid surrounding the cylinder and an error growth can be expected when the thickness of the layer becomes comparable with the distance between the points on the two facing boundaries. This is confirmed by the evolution of mass conservation reported in Figure 4 for different discretizations, whose relevant parameters are summarized in Table 2. Due to the stretching of the free surface, it has been found that, for obtaining refined results up to $t = 2$, only the number $N_{\mathcal{F}}$ of free surface markers needs to be further increased and, for the most refined computation 'f', the final relative error in mass conservation is about 2×10^{-7}.

Even before significant changes in total mass appear, the energy balance at first (center plot in Figure 4), and the force components later on (bottom plot), oscillate when the thickness of the fluid layer surrounding the body starts to be small relatively to markers density. In particular, it is interesting to observe that the check on energy balance is more sensitive, because the oscillations start sooner with respect to mass and forces evolutions. Anyway, the work input and energy growth rate agrees better and better by refining enough the discretization and, for the most refined case, the difference between E_t and W never exceeds 10^{-5} (cf., center right plot in Figure 4). The hydrostatic force component is not included in Figure 4 and, also in this case, a smooth datum can be obtained by increasing $N_{\mathcal{F}} + N_{\mathcal{B}}$. A local analysis is finally performed by plotting in Figure 5 the distance $|\boldsymbol{P}_{\mathrm{j}}(\theta, t) - \boldsymbol{P}_{\mathrm{k}}(\theta, t)|$ of corresponding markers at time t obtained by grid j = e (f) and grid k = d (e), from Table 2. It can be seen that the maximum difference at the end of the simulation between the two most refined grids is at most $\mathcal{O}(10^{-3})$.
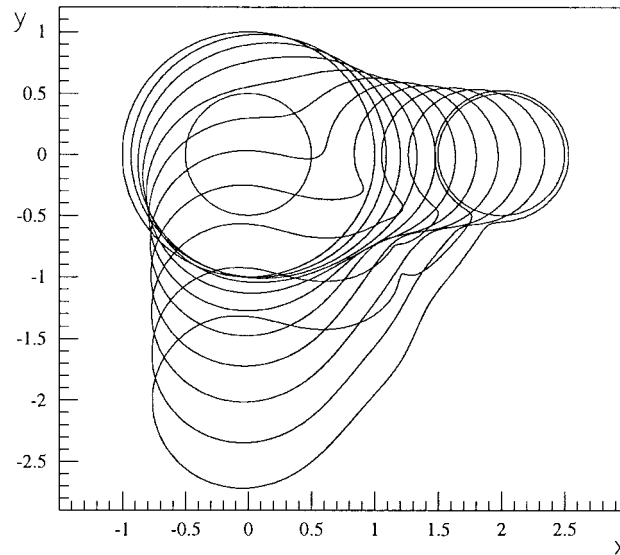
Figure 3. Evolution of the free surface due to the combined action of the gravity and of the sudden horizontal motion, Fr = 1, of the circular cylinder, $\varepsilon = 0.5$ (Case II in the next section). The results are obtained by the most refined discretization of Table 2 and plotted from $t = 0$ up to $t = 2$ with a time interval $\delta t = 0.2$.

5. Results by asymptotic theory and numerical computations

5.1. FREE SURFACE

We now discuss the free surface evolution forced by the motion of the inner cylinder, possibly combined with the action of the gravity. From Equation (46), we note that the highest Fourier mode $\cos 3(\theta - \alpha)$ has vanishing amplitude not only in the limit $\varepsilon \to 1$ but also at a smaller radius $\varepsilon \simeq 0.8688$, while its maximal amplitude occurs for $\varepsilon \simeq 0.4545$. This shows that the most important short-wavelength deformations of the boundary occur when the non-dimensional radius ε is about 0.5. For smaller radii, the inner cylinder is too far from the boundary to be able to promote short-wavelength deformations. For larger radii, the tendency towards locally uniform thin-layer flow will impede the evolution of short-wavelength deformations.

On this ground, we consider the cylinder radius $\varepsilon = 0.5$ as a privileged test-case for discussing the limit of validity of our analytical theory and comparing against the numerical fully nonlinear findings. In Case I, Figure 6, we first consider forced horizontal motion and zero gravity. Successive snapshots of the free surface by analytical third-order theory, ●, and numerical computations, solid lines, are reported in the left-hand plot. As time passes, the fluid packet becomes more and more asymmetric in the direction of the motion. A film of fluid, surrounding the cylinder, gradually appears: its angular extent grows in time while thickness slowly diminishes as more and more mass is left behind to feed a bulge of fluid. The agreement between the two solutions is quite good at least up to $t = 0.4$. Small differences start to appear for $t > 0.6$ which, eventually, become unacceptable for larger times. As previously discussed, mass conservation is only approximately satisfied by the asymptotic solution. In particular, this is illustrated through the time evolution of the area inside the free surface $\mathcal{F}$ reported in Table 3 with that of other cases discussed below.
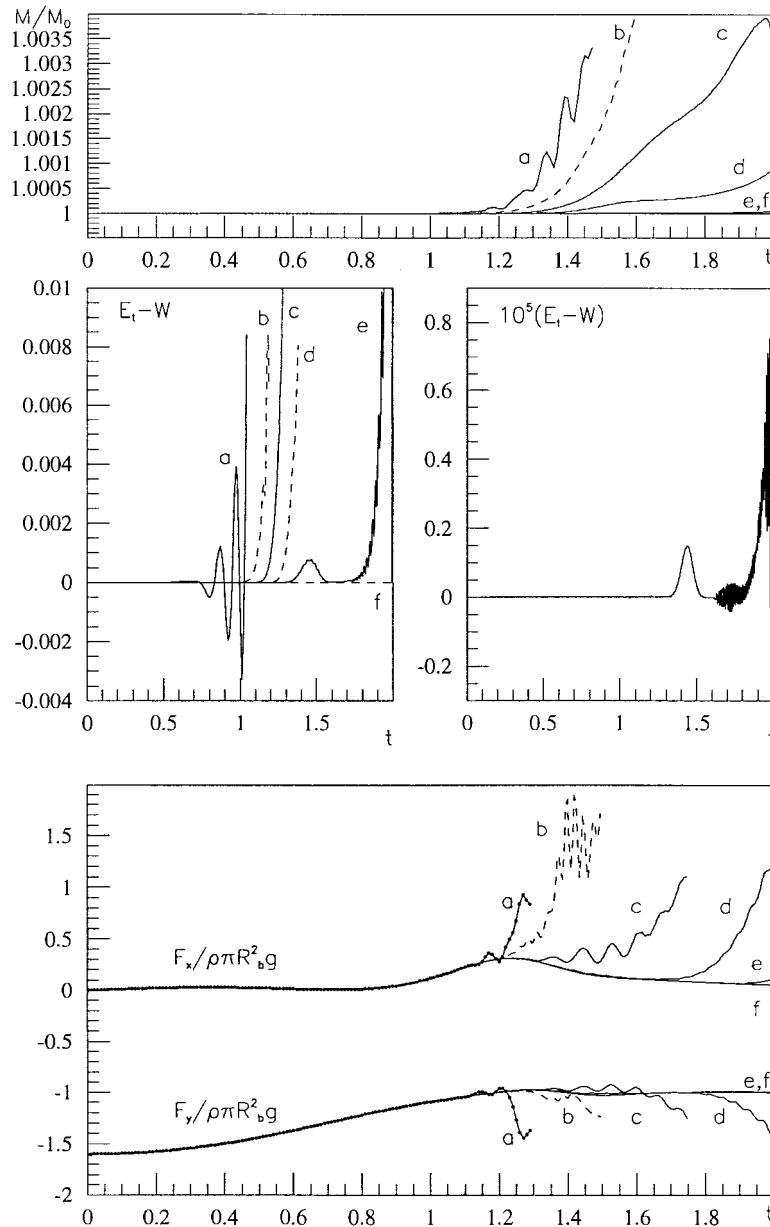
Figure 4. Time evolution of mass (top), difference between rate of energy variation E_t and power input W (center) and force components without F_{-1} (bottom) for the case of Figure 3. The different lines refer to 'a' through 'f' discretizations (cf. Table 2). The center right plot refers only to grid 'f', where the energy imbalance is magnified by a factor 10^5.

A more quantitative comparison between the two solutions is reported in the right-hand plot of Figure 6 through the time evolution of the differences Δx, Δy between the coordinates of Lagrangian markers (in the numerical solution) and of analytical points with same angular position $\theta(t)$. As time approaches unity, Δx, Δy roughly grow as t^3. For a longer time, the nonlinear solution starts to be a multi-valued function of θ and this comparison cannot be performed.
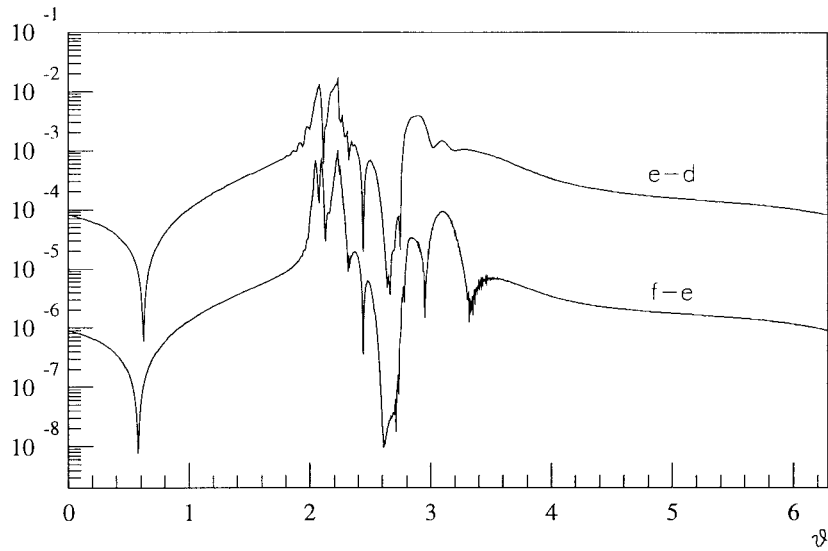
Figure 5. Distance between the positions of free surface markers at $t = 2$ obtained by grid 'e' and 'd' and by 'f' and 'e' as a function of the initial azimuthal coordinate θ.
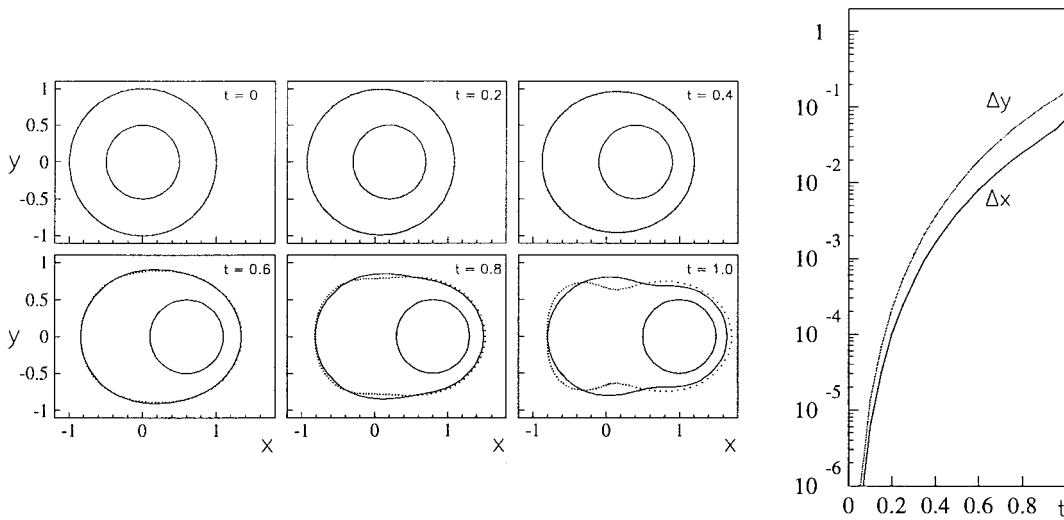

Figure 6. Case I. Evolution of the fluid packet forced by the horizontal motion with unit velocity of the inner cylinder, $\varepsilon = 0.5$. Zero-gravity case, Fr $= \infty$. Left: fully nonlinear (solid lines) and third-order analytical (•) free surface contours for $t = 0, \dots, 1 \ (0.2)$. Right: time evolution of the maximum difference Δx, Δy between the small time expansion and the fully nonlinear solution.

Table 3. Time evolution of the area inside the free surface $\mathcal{F}$ obtained by the small time expansion.

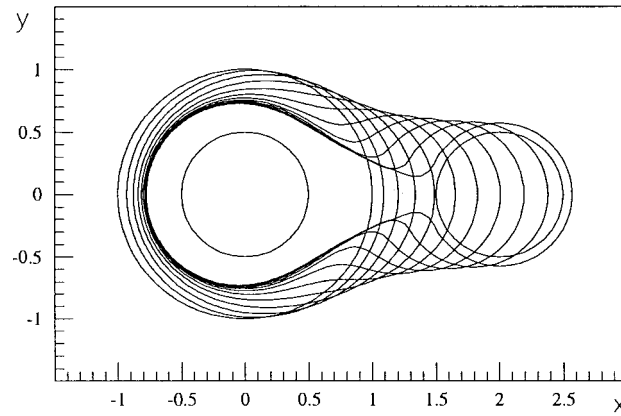| t	0·0	0·2	0·4	0·6	0·8	1·0
Case I	3·14159	3·14161	3·14209	3·14572	3·16164	3·21255
Case II	3·14159	3·14184	3·14594	3·16667	3·23432	3·41027
Case IV	3·14159	3·14176	3·14325	3·14641	3·14967	3·15420

Figure 7. Case I. Free surface evolution up to $t = 2$; time interval between two successive configurations $\delta t = 0.2$. Only initial and final positions of the cylinder are reported.
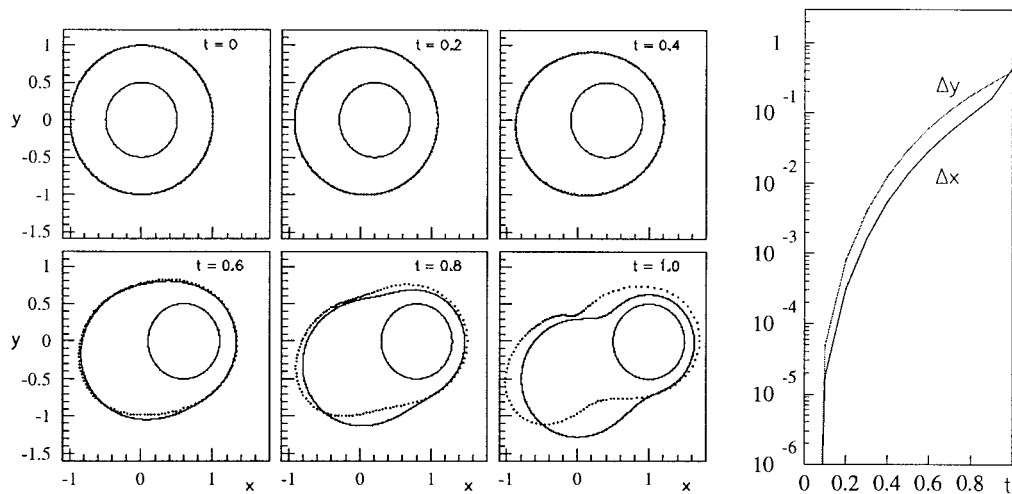

Figure 8. Case II. Evolution of the fluid packet forced by the rightward horizontal motion, Fr $= 1$, of the cylinder, $\varepsilon = 0.5$. Left: fully nonlinear (solid lines) and third-order analytical ($\bullet$) free surface contours for $t = 0, \ldots, 1$ (0.2). Right: time evolution of the maximum difference Δx, Δy between the analytical third-order contours and the numerical results.

The (numerical) evolution up to $t = 2$ is plotted in Figure 7. As the cylinder advances, the thickness of the fluid layer surrounding the body shrinks and remains connected to the bulk of fluid left behind through a feeding portion with decreasing thickness. At this stage, small fluid thickness and high curvature of the free surface would probably imply a significant role of surface tension and viscous effects which are not presently modeled. Therefore, though convergence tests and checks through quantities (55)–(57) are still quite satisfactory, the simulation is not prolonged anymore.

In the absence of gravity and because of the symmetry of the initial conditions, the problem is indifferent to the direction of motion. For finite Froude numbers we need also to investigate the effect of the direction of motion. The combined effect of rightward motion and gravity, Case II, has been anticipated in Figure 3 of previous section. Here, the initial evolution is reported and compared with our theoretical results, Figure 8. The bulge of fluid left behind
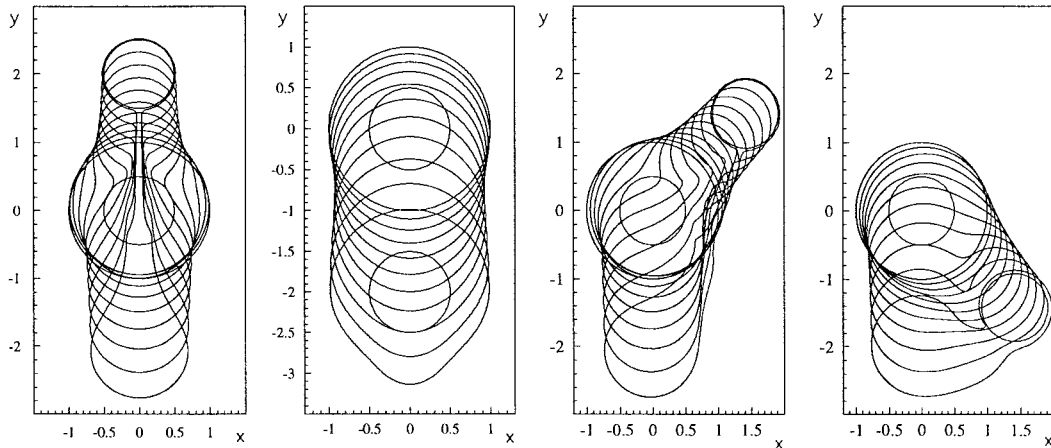
Figure 9. Shape of fluid packet for inner cylinder radius, $\varepsilon = 0.5$, with vertical and oblique motion, Fr $= 1$. Surface shape shown with time increments 0.2. From left to right: upward motion ($\alpha = \pi/2$, Case III), downward motion ($\alpha = -\pi/2$, Case IV), oblique upward motion ($\alpha = \pi/4$, Case V), oblique downward motion ($\alpha = -\pi/4$, Case VI).
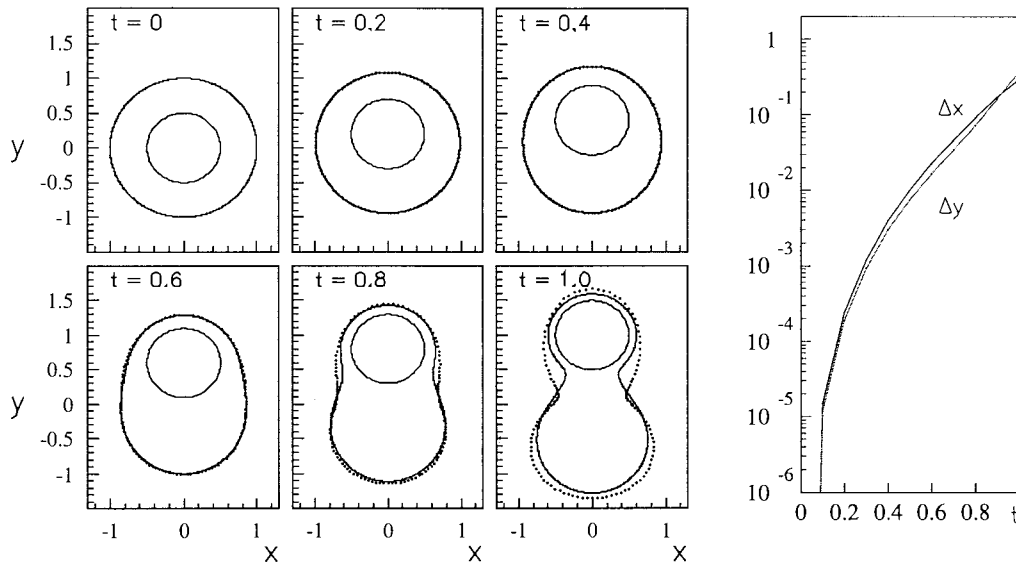

Figure 10. Case III. Evolution of the fluid packet forced by vertical upward motion, Fr $= 1$, of the inner cylinder, $\varepsilon = 0.5$. Left: the fully nonlinear (solid lines) and third-order analytical (•) free surface contours for increasing time. Right: time evolution of the maximum difference Δx, Δy between the small time expansion and the fully nonlinear solution.

starts falling down. This tends to increase the mass imbalance of the asymptotic expansion, as can be seen in Table 3. Accordingly, the difference between numerical and analytical solutions are somewhat larger than in the gravity-less case. From Figures 3 and 7 one can compare cases with and without gravity on a longer time scale. With gravity, larger free-surface deformations are observed, the fluid film is thinner, and the tail of the bulge is narrower and deformed by undulations.

Figure 9 collects cases III through VI with vertical and oblique motions of the cylinder and $\varepsilon = 0.5$, which is our preferred example from an analytical point of view. For upward
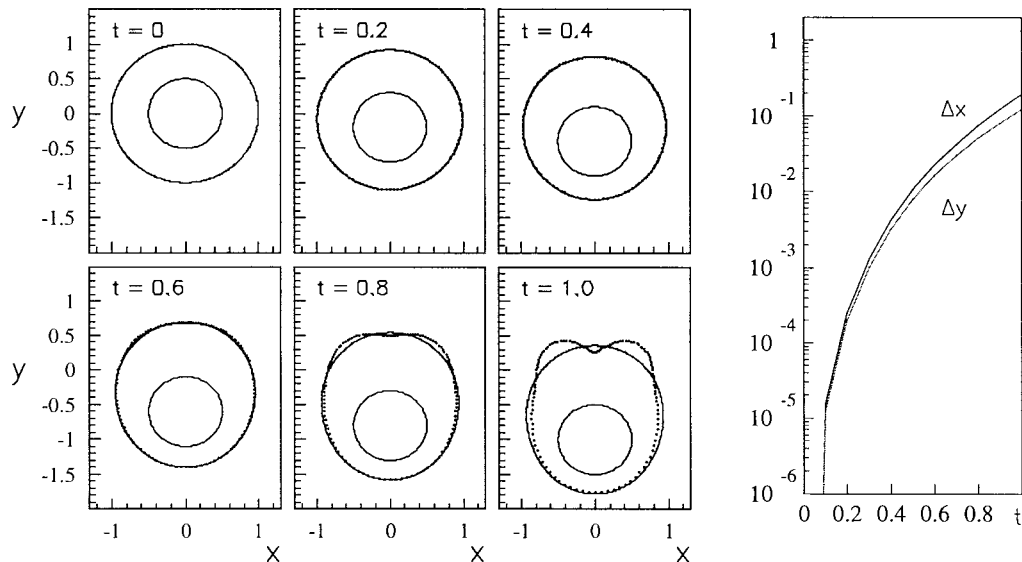
Figure 11. Case IV. Evolution of the fluid packet forced by vertical downward motion, Fr $=$ 1, of the inner cylinder, $\varepsilon = 0.5$. Left: the fully nonlinear (solid lines) and third-order analytical (•) free surface contours for increasing time. Right: time evolution of the maximum difference Δx, Δy between the small time expansion and the fully nonlinear solution.

motion a bulge of fluid is quickly left behind, and a fluid layer of almost uniform thickness will surround $\mathcal{B}$. As time passes, this layer becomes extremely thin. For an oblique upward motion we also get a thin layer surrounding the cylinder, with a freely falling drop left behind. Oblique downward motion gives a less pronounced separation of the falling drop, but still the drop will experience almost free fall. The vertical downward motion differs significantly from the previous cases because the free surface tends to preserve for a longer time the circular shape. Eventually, the bulk of fluid becomes faster than the body and a bulge starts to appear ahead of the cylinder.

For Case III and Case IV, we report a more detailed comparison between the analytical and numerical results (cf., Figures 10–11, respectively). In both cases serious deviations of the analytical solution from the numerical one start to appear for $t > 0.5$. For upward motion of the cylinder, Case III, the analytical solution predicts too thick fluid film close to the cylinder. For downward motion, Case IV, a qualitative error appears in the analytical prediction as time approaches one: the formation of a dip above the cylinder. No such dip is detectable in the numerical computations, even for larger times. It is interesting to note that the mass defect in the asymptotic series is very small in this case (cf., Table 3). This clearly shows that mass balance gives no guarantee of local convergence of the small time expansion.

In Appendix B we have solved the full third-order problem in a coordinate system following the solid cylinder in its forced motion. Then the geometric nonlinearity disappears, and the solution procedure is simpler because all flow nonlinearities appear at the free surface only. However, in this case, the agreement of the free surface shape with the fully nonlinear numerical solution is relatively poor compared with the much better solution in the system at rest. We conclude that the concept of geometric nonlinearity is advantageous for following the nonlinear free surface flow analytically as far as possible before the expansion breaks down. To give some ideas on why the expansion in the system at rest is better than the one in the
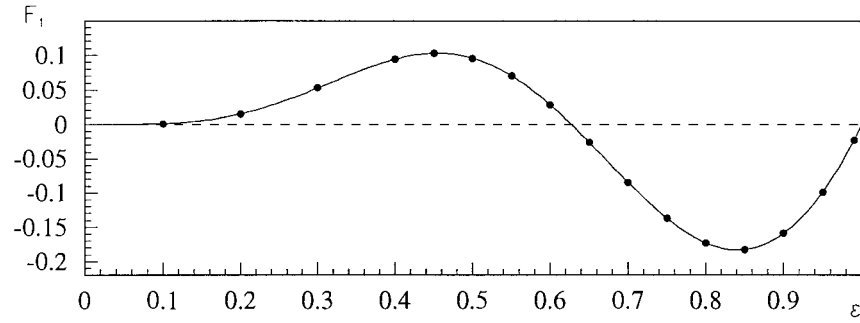
Figure 12. First-order contribution F_1 to force (solid line) as a function of the cylinder radius ε. Symbols • report the slope of $F_x(t)$ in the limit $t \to 0$ for $Fr^{-2} = 0$ and cylinder moving from left to right with unit velocity.

moving system, we take a close look at Figure 10: the small-time expansion in the system at rest is very good up to $t = 0.6$, quantitatively reasonable at $t = 0.8$, and still of qualitative value at $t = 1$. In the last case the asymptotic expansion gives a thin layer on top, the shrinking waist in the middle has an almost correct width, and the bulge below has a reasonable shape. As a contrast, the analysis of Appendix B gives no meaningful solution at all at $t = 1$. The correct solution would in fact be a double-valued function for $R(\theta)$ in the moving system. The shrinking waist effect would be impossible to describe. So we have seen that the description in the system at rest stays reasonable for greater time than the description in the moving system. Then it is likely to have a better convergence for smaller times as well.

5.2. HYDRODYNAMIC FORCE

In our small time expansion analysis, the hydrodynamic force is expressed in the form $\boldsymbol{F}(t) = \boldsymbol{F}_{-1}\delta(t) + H(t)(\boldsymbol{F}_0 + \boldsymbol{F}_1 t + \dots)$, and exact expressions for $\boldsymbol{F}_{-1}$, $\boldsymbol{F}_0$ are given in Section 3. In particular, $\boldsymbol{F}_0$ has already been used to validate the numerical procedure and a complete agreement is achieved. This is reasonable because the solution for $t = 0$ is exact in the fully nonlinear sense. To evaluate the impulsive force from the fluid packet, $\boldsymbol{F}_{-1}$, the boundary value problem for $\dot{\boldsymbol{u}}$ is solved by assuming a unit body acceleration and evaluating the corresponding load. The obtained result fully recovers the exact formula. The same force component could be evaluated using the definition $\boldsymbol{F}_{-1} = \int_{\mathcal{B}} \Phi_0 \boldsymbol{\nu} dS$, solving the velocity field for $t = 0$ and integrating the tangential fluid velocity at the body to obtain the potential Φ_0.

The first-order force $\boldsymbol{F}_1$, Equation (48), is defined as positive in the direction of motion. In particular (cf., Figure 12), $F_1 > 0$ for $0 < \varepsilon < 0.6266$, i.e., favoring the cylinder to move. A change of sign is then observed so that the first-order force is directed against the velocity of the cylinder in the range $0.6266 < \varepsilon < 1$. Summing up, the first-order force expresses a tendency that a thin fluid layer maintains its inertial grip on the cylinder, while a thick fluid layer collects itself as a downstream packet that starts repelling the cylinder. These two tendencies are exactly balanced for $\varepsilon \simeq 0.6266$ so that $F_1 = 0$. More obviously, the first-order force is zero both for $\varepsilon = 0$ and $\varepsilon = 1$; the two terms in Equation (47) do not satisfy these conditions separately, but as a sum. A numerical check is achieved by considering the gravity-less flow generated by a cylinder moving from left to right. Several cylinder radii ε are considered and the 'slope' of the hydrodynamic force for $t \to 0$ is numerically evaluated by using a very small time step and a second-order centered derivative. Numerical results, • plotted in Figure 12, apparently recover the analytical solution, solid line, for all the considered radii.
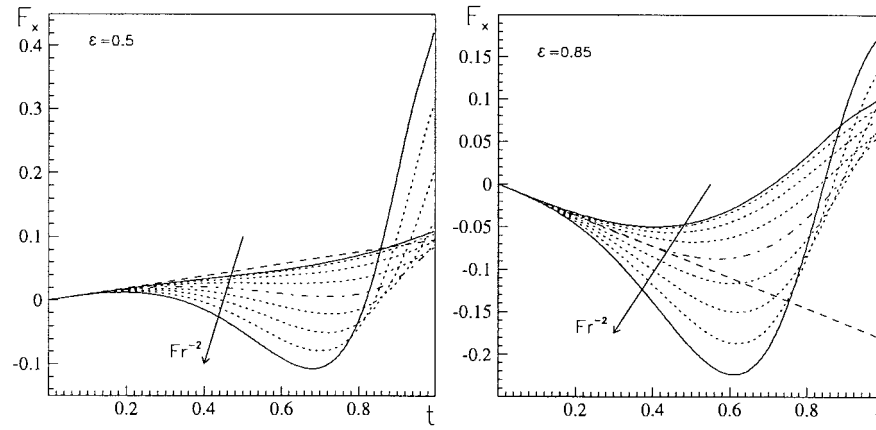
Figure 13. Time evolution of horizontal force component for gravity $Fr^{-2} = 0, \ldots, 2.0 \, (0.25)$; the extreme values are denote by solid lines, $Fr^{-2} = 1$ by dash-dot lines and arrows show increasing gravity. Left: $\varepsilon = 0.5$. Right: $\varepsilon = 0.85$. Dashed lines report the corresponding analytical slope F_1.

According to the present theory, the force acting on the body should be gravity-independent asymptotically for small times. It is then interesting to study the effect of finite Froude numbers on loads for finite times. To the purpose, we consider the case of horizontal motion for which $\boldsymbol{F}_1$ gives the only non-zero horizontal component ($\boldsymbol{F}_{-1}$ disappears for $t > 0^+$ and $\boldsymbol{F}_0$ is always vertical). In Figure 13, the time evolution of the numerical F_x is plotted for increasing gravity, for $\varepsilon = 0.5$ (left-hand plot) and $\varepsilon = 0.85$ (right-hand plot). For both radii, the corresponding analytical prediction is represented by the dashed line. For the smallest ε, this gives a reasonable estimate of the gravity-less solution over the entire interval of time considered. More generally, for all the considered Fr, the initial behaviour of F_x is predicted very well by our asymptotic theory at least for $t < 0.2$, after that $F_x(t)$ departs from the linear behaviour. For small gravity, the horizontal force component still remain positive (i.e., favoring the body motion) while, for Fr^{-2} large enough, the force becomes negative, reaches a minimum and, eventually, starts to grow: the greater the gravity, the faster the growth.

For $\varepsilon = 0.85$ and $Fr = \infty$, $F_x(t)$ significantly deviates from the analytical result and, in general, for $Fr > 1$ the analytical prediction overestimates in magnitude the numerical one. As gravity Fr^{-2} increases from zero to unity, $F_x(t)$ behaves more and more linearly in time: for $Fr = 1$ (dash-dot line) the horizontal component is well predicted by the asymptotic theory up to $t \simeq 0.4$, and after that deviates sharply. For $Fr < 1$, the behaviour is qualitatively similar to the case $\varepsilon = 0.5$, i.e., the force sharply grows, becoming positive, after a negative minimum has been attained.

In spite of the above deviations of our analytical expression for the force from the numerical results, the corresponding analytical description of the surface agrees well up to $t \simeq 0.5$. This is reasonable because the last term actually included in Equation (13) is $\boldsymbol{F}_1$. Therefore the presented results are two orders less accurate than those given for R. The evaluation of the next term, $\boldsymbol{F}_2$, requires the solution of the third-order potential, Φ_3, and would produce the fourth-order deformation, R_4.

5.3. LEADING GRAVITATIONAL EFFECTS IN THE THIRD-ORDER POTENTIAL

The gravity-dependent terms in the third-order solution for moving body express the leading-order nonlinear interaction between gravity and forced flow. The purely gravitational self-interaction enters the nonlinear problem in the fourth-order deformation. We now derive the fourth-order free surface for a cylinder at rest: this represents the leading nonlinear self-interaction in a purely gravitational flow but gives also the dominating contribution in case of body motion when Fr $\ll$ 1. This will allow us to derive a non consistent fourth-order approximation in case of slow body motions.

If there is no forced velocity, $W = 0$, our time unit vanishes. Therefore, we have to apply the gravitational time scale $(R_{\mathscr{F}}/g)^{1/2}$ and the consistently redefined Froude number equals one. In the derivation below, we maintain Fr because we will apply the fourth-order correction term also for Fr $\ll$ 1.

In case of a fixed cylinder, the dynamic and kinematic conditions on the free surface $r = 1$ at each order read

$$\Phi_0 = 0 \qquad\qquad\qquad R_1 = 0 \tag{58a}$$

$$\Phi_1 = -\frac{1}{\mathrm{Fr}^2}\sin\theta \qquad\qquad 2R_2 = \frac{\partial\Phi_1}{\partial r} \tag{58b}$$

$$\Phi_2 = 0 \qquad\qquad\qquad R_3 = 0 \tag{58c}$$

$$6\Phi_3 = -\frac{2}{\mathrm{Fr}^2}R_2\sin\theta - \frac{1}{\mathrm{Fr}^4}\cos 2\theta - 8R_2^2 \quad 4R_4 = \frac{\partial\Phi_3}{\partial r} + R_2\frac{\partial^2\Phi_1}{\partial r^2} - R_2'\frac{\partial\Phi_1}{\partial\theta} \tag{58d}$$

respectively, while

$$\frac{\partial\Phi_j}{\partial r} = 0 \quad r = \varepsilon \quad (j = 0, 1, 2, 3) \tag{59}$$

are the corresponding boundary conditions on the body. The first and third-order elevations are identically zero and all the potentials Φ_j are solution of a Type I problem in the Appendix A. Hence the second-order elevation is:

$$R_2 = -\frac{1}{2\mathrm{Fr}^2}\frac{1-\varepsilon^2}{1+\varepsilon^2}\sin\theta. \tag{60}$$

This fixes Φ_3 on $r = 1$ and, by using again Equation (A3), the fourth-order surface deformation is determined as:

$$R_4 = -\frac{1}{16\mathrm{Fr}^4}\left(\frac{1-\varepsilon^2}{1+\varepsilon^2}\right)^2 - \frac{1}{48\mathrm{Fr}^4}\frac{(1-\varepsilon^2)(3+21\varepsilon^2+11\varepsilon^4+5\varepsilon^6)}{(1+\varepsilon^2)^2(1+\varepsilon^4)}\cos 2\theta. \tag{61}$$

This takes into account the leading nonlinear self-interaction due to gravity, and also a fourth-order compensation for the mass defect due to the second-order solution. In [1], the authors gave only a second-order solution for the gravitational release of a half-cylinder of fluid. We also note that, according to our analytical theory, the fourth-order displacement is different from zero in the limit $\varepsilon \to 0$. In this limit case, the second-order displacement represents free fall.

In Figure 14, we show the comparison between the above analysis (dashed lines) and our numerical computations (solid lines). From left to right, three different cylinder radii are
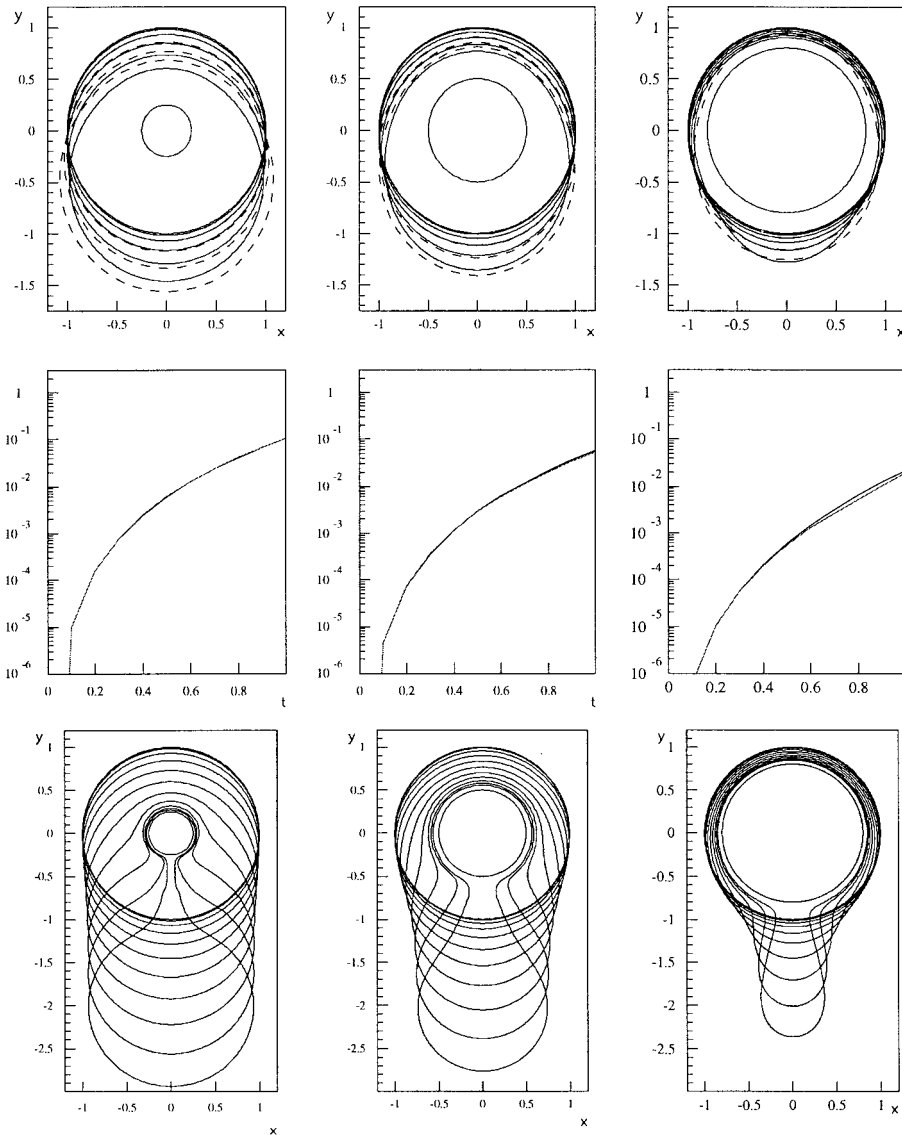
Figure 14. Gravity release of fluid packet surrounding a circular cylinder at rest. (ε = 0·2, 0·5, 0·8 from left to right, respectively). Top plots: the numerical solution of the exact problem, solid lines, is compared with the fourth-order asymptotic result, dashed lines, for time t = 0, ..., 1·2 (0·2). Center plots: time evolution of the the maximum radial difference between the two solutions. Bottom plots: evolution up to t = 2 by numerical simulation.

considered (ε = 0·2, 0·5 and 0·8, respectively). For the smallest one, the lower half of the fluid contour falls freely almost like a rigid body, while the upper half is strongly impeded by the interior solid boundary. For ε = 0·5 or larger, all the fluid contour has a significant impeded motion due to the presence of the cylinder. The time evolution of the maximum difference Δx, Δy (center plots) shows that the error growth now is behaving as t^4 and is (slightly) smaller for the largest ε. In all cases, on a longer time scale, the fluid flows into a drop below the body at the expense of a circular layer of liquid surrounding $\mathcal{B}$ which becomes thinner and thinner.
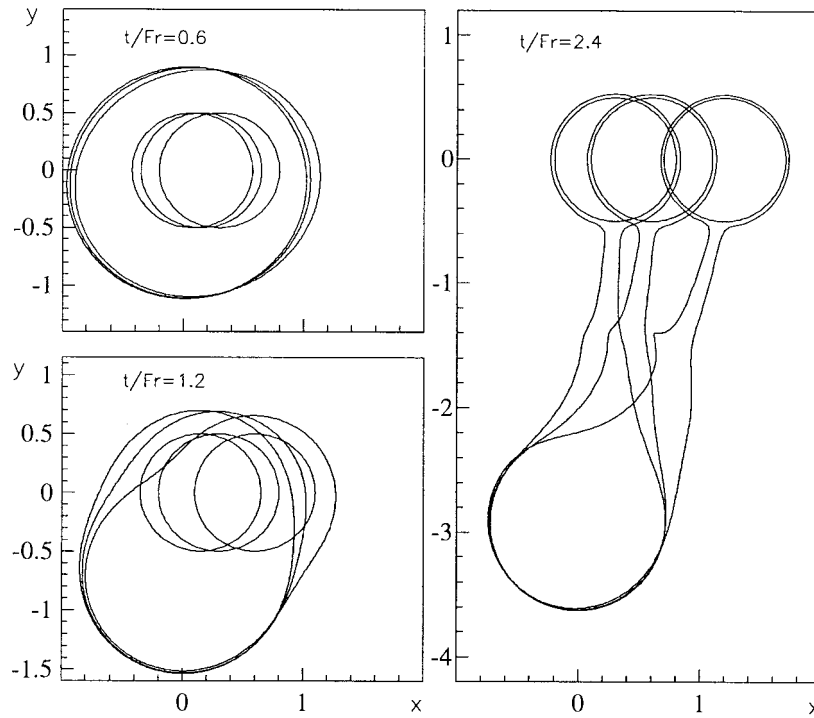
Figure 15. Comparison of free surface for Fr $= 0{\cdot}125, 0{\cdot}25, 0{\cdot}5$ in case of rightward horizontal motion of the cylinder ($\varepsilon = 0{\cdot}5$). The time is scaled by $1/$Fr. In each plot, the three different cases can be distinguished by the location of the cylinder (larger displacement for larger Froude number).

In the purely gravitational case with the inner cylinder at rest, all forces are vertical and the zeroth-order force on the cylinder has already been given by Equation (33). It is obvious that all forces are zero to odd orders in time. Our calculation shows that the second-order force is also zero. Thus the leading time-dependent force will be of fourth-order in time, but its expression is very complicated and will be omitted here. It seems likely that this fourth-order force will be positive. This means that the downward added-mass force will stay almost constant until it starts dropping very quickly about $t = 1$.

For Fr^2 small enough, the fourth-order term R_4 represents also the dominating gravitational self-interaction term in the case of body motion. On this ground, we finally consider in Figure 15 the case of rightward horizontal motion for Fr $= 0{\cdot}125, 0{\cdot}25$ and $0{\cdot}5$. Three different free surface configurations are plotted for the same normalized time t/Fr. The motion of the falling drop scales with Froude number, while closer to the body the fluid motion is dominated by the forced displacement. It is also interesting to observe that the thickness of the fluid layer is essentially the same in the three cases. We computed the (consistent) third-order solution and a non consistent solution by adding also the fourth-order correction R_4. For both of them the evolution in time of the corresponding maximum difference Δx with respect to the numerical solution is reported in Figure 16. It appears that the behaviour of the not consistent asymptotic solution (solid lines) is slightly better than the consistent third-order solution. Further, when comparing errors using the stretched time $t/$Fr we could also see that Δx is smaller for smaller Fr. This is because we have included the fourth-order term which is dominating for small Froude numbers.
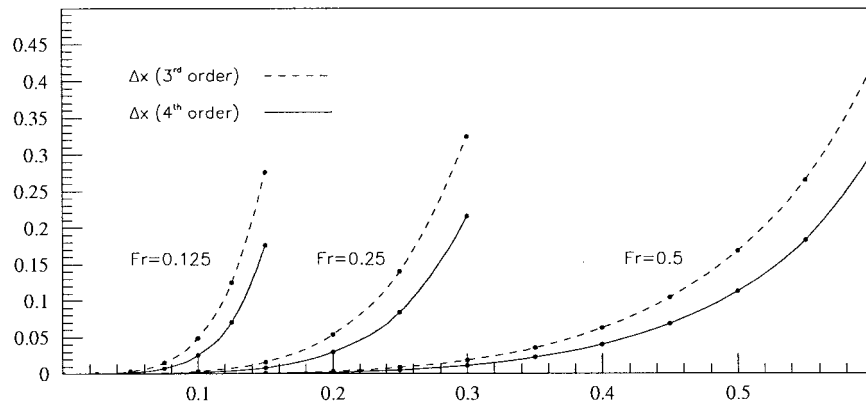
Figure 16. Time evolution of the maximum difference Δx between numerical simulation and asymptotic theory for the cases of Figure 15. Dashed lines: third-order solution. Solid lines: third-order with inconsistent fourth-order correction.

6. Summary and conclusions

A solid circular cylinder surrounded by a uniform fluid layer is impulsively put in motion in a gravity field. The resulting nonlinear free-surface flow is studied analytically by an asymptotic expansion in time. The analysis is completed by the numerical solution of the exact problem.

The asymptotic analysis is exact to third order as $t \to 0$ and includes the leading-order interaction between flow forced by the moving body and gravitational flow.

Closed-form formulas, valid for an arbitrary radius of the inner cylinder, are given for free surface, potential and hydrodynamic force acting on the body. A fourth-order analysis of gravitational self-interaction is also performed for the case of an inner cylinder at rest.

An accurate numerical boundary-integral-equation method has been adopted to provide reference solutions to the exact problem. On this ground, the time-scale of validity of our analytical solution is assessed and, on the longer range, some interesting features are evidenced.

Comparisons with the numerical solution show that the three-term asymptotic expansion for the free surface is quite accurate up to $t \simeq 0.5$, assuming small or moderate gravitational effect (Time equals to 0.5 corresponds to a body displacement of half the initial radius of the fluid packet).

The considered problem is related to the late stages of cylinder-exit experiments in [18, Figures 5.1–5.2], also reported in [19, pp 309–312]. In those experiments, just after a rapidly moving cylinder has risen above the undisturbed water level, an almost uniform fluid layer surrounding the body is observed. When the cylinder finally loses its connexion with the bulk fluid below, about two thirds of its periphery is covered by a water film. It is likely that the gross evolution of the fluid packet will be independent of the main fluid domain below because the stagnant pressure in the wake past the cylinder cuts off all pressure-transmitted communication between the surrounding fluid film and the main fluid domain below. The main features of such flows are recovered analytically in [7] for the submerged cylinder model, and appears also in the present problem. Apparently, geometric nonlinearity plays an important role in the formation of this uniform fluid layer, which cannot be understood by linear theory alone.

More extended comparisons with water exit experiments are hampered by the occurrence of flow separation. In the experiments mentioned above, the cylinder motion starts far enough

from the free surface, and separation has enough time to develop. In [20] data are shown for the evolution of the drag for impulsive motions of a cylinder in infinite fluid at high Reynolds numbers. Both constant velocity and constant acceleration are given. As long as the cylinder displacement is smaller than its own radius, the viscous drag is small. This means that separation did not have time to develop and we argue that the present inviscid irrotational model will be reasonably good for a fluid of small viscosity as long as the cylinder displacement is not greater than its radius.

Finally, it is likely that the velocity field in the fluid packet surrounding the cylinder after the exit is far from the quiescent one assumed in our work. Therefore, a small-gravity environment, where the free surface body interaction starts abruptly, could give better conditions for experimental testing of the present model.

Hydrodynamic forces have also been analyzed. The leading-order force is the singular added-mass force. The zeroth-order force is purely gravitational, and it is similar to the impulsive added-mass force. These force components are exact also in the context of a fully nonlinear analysis at $t = 0^+$, and can be used to check numerical methods. In particular, they are well recovered by the adopted numerical method.

The results for the first-order force show an interesting behaviour: during the first stage of motion, small cylinders experience a first-order repelling force, *i.e.*, favoring the motion, while larger cylinders experience an impeding force. This is quantitatively confirmed by the numerical solutions, though on a longer time scale large deviations from the numerical solution are observed. In particular, the latter is characterized by large force oscillations with changing sign.

The numerical method is able to follow large deformations of the free surface. Actually, for very thin fluid layers and sharp deformations of the free surface, viscosity and surface tension should play a relevant role. Such effects are not presently modeled.

Acknowledgements

Appendix A. Two basic boundary-value problems

There are two basic types of boundary-value problems to each order in the small-time expansion.

Type I problem

Let the potential be given at the outer boundary, with zero normal derivative at the inner boundary, *i.e.*

$$\phi = \cos n(\theta - \beta), \quad r = 1, \quad \frac{\partial \phi}{\partial r} = 0, \quad r = \varepsilon, \tag{A1}$$

n being any integer and β an arbitrary phase angle. The solution of this boundary-value problem is:

$$\phi = \frac{r^n + \varepsilon^{2n} r^{-n}}{1 + \varepsilon^{2n}} \, \cos n(\theta - \beta).$$

(A2)

In the calculation of the surface shape, we need its normal derivative at the outer boundary:

$$\frac{\partial \phi}{\partial r} = n \frac{1 - \varepsilon^{2n}}{1 + \varepsilon^{2n}} \, \cos n(\theta - \beta), \quad r = 1.$$

(A3)

We evaluate the function and its gradient at the inner boundary:

$$\phi = \frac{2\varepsilon^n}{1 + \varepsilon^{2n}} \, \cos n(\theta - \beta), \quad \frac{1}{\varepsilon} \frac{\partial \phi}{\partial \theta} = -\frac{2n\varepsilon^{n-1}}{1 + \varepsilon^{2n}} \, \sin n(\theta - \beta), \quad r = \varepsilon.$$

(A4)

The normal derivative is given in the second of Equations (A1) as zero.

Type II problem

Let the potential be specified by its normal derivative at the inner boundary, while being zero at the outer boundary. We consider here a Fourier component as the prescribed potential. We thus have:

$$\psi = 0, \quad r = 1, \qquad \frac{\partial \psi}{\partial r} = \cos n(\theta - \beta), \quad r = \varepsilon.$$

(A5)

The solution of this boundary-value problem is:

$$\psi = \frac{1}{n} \frac{r^n - r^{-n}}{\varepsilon^{n-1} + \varepsilon^{-n-1}} \, \cos n(\theta - \beta)$$

(A6)

valid for non-zero integers, while for $n = 0$ we have the solution:

$$\psi = \varepsilon \, \log r.$$

(A7)

The normal derivative at the outer boundary is given for any integer n by the formula:

$$\frac{\partial \psi}{\partial r} = \frac{2}{\varepsilon^{n-1} + \varepsilon^{-n-1}} \, \cos n(\theta - \beta), \quad r = 1.$$

(A8)

One may need to evaluate the function and its gradient at the inner boundary. We have:

$$\psi = -\frac{\varepsilon}{n} \frac{1 - \varepsilon^{2n}}{1 + \varepsilon^{2n}} \, \cos n(\theta - \beta), \quad \frac{1}{\varepsilon} \frac{\partial \psi}{\partial \theta} = \frac{1 - \varepsilon^{2n}}{1 + \varepsilon^{2n}} \, \sin n(\theta - \beta), \quad r = \varepsilon.$$

(A9a)

for non-zero integers n, and

$$\psi = \varepsilon \, \log \varepsilon, \qquad \frac{1}{\varepsilon} \frac{\partial \psi}{\partial \theta} = 0, \quad r = \varepsilon,$$

(A9b)

for $n = 0$, respectively.

Appendix B. Asymptotic theory in a coordinate system following the cylinder motion

The asymptotic theory in the main text is performed in a coordinate system which is at rest with the fluid before the motion starts. In this appendix, we will develop an alternative small-time expansion in a coordinate system that follows with the motion of the inner cylinder. Then the body boundary condition is zero normal velocity at all times. Thus the concept of geometric nonlinearity disappears, and we want to find out whether this makes the convergence of the small-time expansion better or worse. We preliminary remark that, in the limit case $\varepsilon = 1$ displayed in Figure 2, the asymptotic solution in the moving system will be the exact translating circles, because they are at rest in the considered coordinate system. The boundary conditions at the free surface are exactly the same as in the main text. The only two basic changes are the zero normal velocity at the inner boundary, and the flow due to the change of coordinate system, which is included in the zeroth-order potential. The zeroth-order potential is found by subtracting a uniform flow making the angle $\pi - \alpha$ with the x axis:

$$\Phi_0 = -\frac{r + \varepsilon^2/r}{1 + \varepsilon^2} \cos(\theta - \alpha). \tag{B1}$$

This gives the first-order deformation:

$$R_1 = -\frac{1 - \varepsilon^2}{1 + \varepsilon^2} \cos(\theta - \alpha). \tag{B2}$$

Upon disregarding an insignificant constant, the first-order potential is:

$$\Phi_1 = -\frac{(1 - \varepsilon^2)^2}{4(1 + \varepsilon^2)^2} \frac{r^2 + \varepsilon^4 r^{-2}}{1 + \varepsilon^4} \cos 2(\theta - \alpha) - \frac{r + \varepsilon^2 r^{-1}}{1 + \varepsilon^2} \frac{\sin\theta}{\mathrm{Fr}^2} \tag{B3}$$

and produces the second-order surface deformation:

$$R_2 = -\frac{1 - 4\varepsilon^2 + 2\varepsilon^4 + \varepsilon^8}{4(1 + \varepsilon^2)^2(1 + \varepsilon^4)} \cos 2(\theta - \alpha) + \frac{(1 - \varepsilon^2)\varepsilon^2}{2(1 + \varepsilon^2)^2} - \frac{1 - \varepsilon^2}{2\mathrm{Fr}^2(1 + \varepsilon^2)} \sin\theta. \tag{B4}$$

The second-order potential is:

$$\Phi_2 = \frac{(-1 + \varepsilon^2)^2(-1 + 4\varepsilon^2 + \varepsilon^4 + 2\varepsilon^6)}{4(1 + \varepsilon^2)^4(1 + \varepsilon^4)}\left(r + \frac{\varepsilon^2}{r}\right) \cos(\theta - \alpha) +$$

$$+ \frac{(-1 + 4\varepsilon^2 - 4\varepsilon^4 + \varepsilon^8)}{4(1 + \varepsilon^2)^3(1 + \varepsilon^4)(1 + \varepsilon^6)}\left(r^3 + \frac{\varepsilon^6}{r^3}\right) \cos 3(\theta - \alpha) - \tag{B5}$$

$$- \frac{(1 - 4\varepsilon^2 + 3\varepsilon^4)}{4\mathrm{Fr}^2(1 + \varepsilon^2)^2(1 + \varepsilon^4)}\left(r^2 + \frac{\varepsilon^4}{r^2}\right) \sin(2\theta - \alpha).$$

and leads to the third-order deformation:

$$R_3 = \frac{-1 + \varepsilon^2}{(1 + \varepsilon^2)^2}\left(\frac{\varepsilon^2(-5 + 4\varepsilon^2 + 2\varepsilon^4 + 4\varepsilon^6 + 3\varepsilon^8)}{4(1 + \varepsilon^2)^2(1 + \varepsilon^4)} \cos(\theta - \alpha) + \right.$$

$$+ \frac{2 - 11\varepsilon^2 + 5\varepsilon^4 + 3\varepsilon^6 + 8\varepsilon^8 - \varepsilon^{10} + \varepsilon^{12} + \varepsilon^{14}}{12(1 + \varepsilon^2)^2(1 + \varepsilon^4)(1 - \varepsilon^2 + \varepsilon^4)} \cos 3(\theta - \alpha) + \tag{B6}$$

$$\left. + \frac{1 - 2\varepsilon^2}{6\mathrm{Fr}^2} \sin\alpha - \frac{\varepsilon^2(7 + 2\varepsilon^2 + \varepsilon^4)}{6\mathrm{Fr}^2(1 + \varepsilon^4)} \sin(2\theta - \alpha)\right).$$

As expected, all deformations are zero in the limit $\varepsilon \longrightarrow 1$.

References

1. W.G. Penney and C.K. Thornhill. The dispersion, under gravity, of a column of fluid supported on a rigid horizontal plane. *Phil. Trans. R. Soc. London* A244 (1952) 285–311.
2. E.B. Dussan V On the spreading of liquids on solid surfaces: static and dynamic contact lines, *Ann. Rev. Fluid Mech.* 11 (1979) 371–400.
3. P.K. Stansby, A. Chegini and T.C.D. Barnes. The initial stages of dam-break flow. *J. Fluid Mech.* 374 (1998) 407–424.
4. D.H. Peregrine. Flow due to a vertical plate moving in a channel. Unpublished note (1972).
5. A.C. King and D.J. Needham. The initial development of a jet caused by fluid, body and free-surface interaction. Part 1. A uniformly accelerating plate. *J. Fluid Mech.* 268 (1994) 89–101.
6. M. Greenhow and S. Moyo. Water entry and exit of horizontal circular cylinders. *Phil. Trans. R. Soc. London* A355 (1997) 551–563.
7. P.A. Tyvand and T. Miloh. Free-surface flow due to impulsive motion of a submerged circular cylinder. *J. Fluid Mech.* 286 (1995) 67–101.
8. P.A. Tyvand. Motion of a vortex near a free surface. *J. Fluid Mech.* 225 (1991) 673–686. (Appendix by R.P. Tong).
9. P. Bassanini, C.M. Casciola, M.R. Lancia and R. Piva. A boundary integral formulation for kinetic field in aerodynamics. Part I: Mathematical analysis. Part II: Applications to unsteady 2D flows. *Eur. J. Mech. B/Fluids* 10/6 (1991) 605–627 and 11/1 (1992) 69–92.
10. A.F. Teles da Silva and D.H. Peregrine. Nonlinear perturbations on a free surface induced by a submerged body: A boundary integral approach. *Eng. Anal. with Bound. Elem.* 7/4 (1990) 214–222.
11. A. Sidi and M. Israeli. Quadrature methods for periodic singular and weakly singular Fredholm integral equations. *J. Scien. Comp.* 3 (1988) 201–231.
12. P. Sonneveld. CGS, A fast Lanczos-type solver for nonsymmetric linear systems. *SIAM J. Sci. Stat. Comput.* 10/1 (1989) 36–52.
13. G. Graziani and M. Landrini. Application of multipoles expansion technique to two-dimensional nonlinear free surface flows. *J. Ship Res.* 43/1 (1999) 1–13.
14. J.W. Dold and D.H. Peregrine. An efficient boundary integral method for steep unsteady water waves. In: K.W. Morton and M.J. Baines (eds), *Numerical Methods for Fluid Dynamics II*, Oxford University Press (1986) 671–679.
15. J.W. Dold. An efficient surface integral algorithm applied to unsteady gravity waves. *J. Comp. Phys.* 103 (1992) 90–115.
16. M.S. Longuet-Higgins and E.D. Cokelet. The deformation of steep surface waves on water. I A numerical method of computation. *Proc. R. Soc. London* A350 (1976) 1–26.
17. G.R. Baker and M. Shelley. Boundary integral methods for multi-connected domains. *J. Comp. Phys.* 64 (1986) 112–132.
18. M. Greenhow and W.-M. Lin. *Nonlinear free surface effects: experiments and theory*. MIT, Dept. of Ocean Engineering, Report 83–19 (1983).
19. O.M. Faltinsen. *Sea Loads on Ships and Offshore Structures*. Cambridge: Ocean Technology series (1990), 328 p.
20. T. Sarpkaya and M. Isaachson. *Mechanics of Wave Forces on Offshore Structures*. New York: Van Nostrand Reinhold (1981) 651 p.